CeO$_2$ Modulates the Electronic States of a Palladium Onion-Like Carbon Interface into a Highly Active and Durable Electrocatalyst for Hydrogen Oxidation in Anion-Exchange-Membrane Fuel Cells

Jimodo J. Ogada, Adewale K. Ipadeola, Patrick V. Mwonga, Aderemi B. Haruna, Forrest Nichols, Shaowei Chen, Hamish A. Miller, Maria V. Pagliaro, Francesco Vizza, John R. Varcoe, Debora Motta Meira, Daniel M. Wamwangi,* and Kenneth I. Ozoemena*

Cite This: *ACS Catal.* 2022, 12, 7014−7029

Read Online

ACCESS | Metrics & More | Article Recommendations | Supporting Information

ABSTRACT: This study reports the preparation, characterization, and electro-catalytic properties of palladium-based catalysts containing ceria (CeO$_2$) on carbon black (CB) and onion-like carbon (OLC) supports. The electrocatalysts (Pd−CeO$_2$/CB and Pd−CeO$_2$/OLC) exhibit a large specific surface area, pore volume, and small particle size, as well as enhanced interfacial interaction and synergy among Pd, CeO$_2$, and OLC in Pd−CeO$_2$/OLC that are valuable for improved electrocatalysis. The presence of CeO$_2$ in Pd−CeO$_2$/OLC induces *ca.* 7% defects and modifies the electronic structure of the Pd/OLC interface, significantly improving the electrical conductivity due to enhanced charge redistribution, corroborated by density functional theory (DFT) calculations. Pd−CeO$_2$/OLC displays the lowest adsorption energies (H*, OH*, and OOH*) among the series. For the hydrogen oxidation reaction (HOR), Pd−CeO$_2$/OLC delivers significantly enhanced HOR (mass-specific) activities of 4.2 (8.1), 13.2 (29.6), and 15 (78.5) times more than Pd−CeO$_2$/CB, Pd/OLC, and Pd/CB, respectively, with the best diffusion coefficient (*D*) and heterogeneous rate constant (*k*). Pd−CeO$_2$/OLC also displays less degradation during accelerated durability testing. In an anion-exchange-membrane fuel cell (AEMFC) with H$_2$ fuel, Pd−CeO$_2$/OLC achieved the highest peak power density of 1.0 W cm^{-2} at 3.0 A cm^{-2} as compared to Pd−CeO$_2$/CB (0.9 W cm^{-2} at 2.2 A cm^{-2}), Pd/OLC (0.6 W cm^{-2} at 1.7 A cm^{-2}), and Pd/CB (0.05 W cm^{-2} at 0.1 A cm^{-2}). These results indicate that Pd−CeO$_2$/OLC promises to serve as a high-performing and durable anode material for AEMFCs.

KEYWORDS: palladium-based nanocatalysts, ceria (CeO$_2$), onion-like carbons (OLCs), metal−support interaction, DFT calculations, hydrogen oxidation reactions, anion-exchange-membrane fuel cell
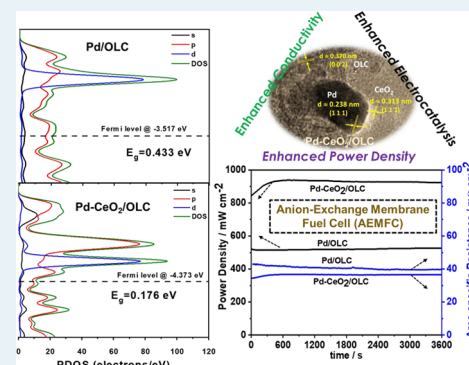
1. INTRODUCTION

Fuel cells are a well-established clean energy conversion technology, efficiently converting the chemical energy contained in a fuel (usually H$_2$) into electrical energy without locally releasing poisonous chemicals or greenhouse gases.[1] The most common low-temperature technology relies upon a proton exchange membrane (PEMFC) and has seen recent commercial implementation in the transportation sector.[2] A younger technology, the anion-exchange-membrane fuel cell (AEMFC) is receiving growing attention due to potential advantages, including a wider range of oxygen reduction catalyst options involving inexpensive (potentially more sustainable) elements, a wider choice of cheaper and more easily fabricated cell and stack components, and less expensive polymer electrolyte options.[3,4] The recent acceleration in the development of AEMFCs that operate in an alkaline environment has sparked renewed interest in the alkaline hydrogen oxidation reaction (HOR) and the considerable challenge of overcoming sluggish HOR kinetics as high Pt

loadings are still required to achieve reasonable performance.[5] Recently, enhancements in HOR activity have been demonstrated through the exploitation of Pd−CeO$_2$ interactions on the nanoscale.[6] Carbon-supported Pd−CeO$_2$ HOR catalysts have been prepared by different synthetic techniques and employed in AEMFCs as an alternative to Pt and PtRu standards.[7,8] Carefully prepared nanostructures of Pd and CeO$_2$ that promote the formation of a Pd−O−Ce interface provide optimal binding of both H$_{ad}$ and OH$_{ad}$ species, aspects which are crucial for enhanced HOR kinetics.[6] CeO$_2$ is used in combination with conductive carbon and must be opportunely designed so that the two phases are chemically interfaced with

overlapping orbitals, such that the conductivity of the carbon is partly transferred to the oxide through the diffusion of freely moving electrons.[6] In such cases, the resulting ternary composite relies on the CeO_2 phase to function as a promoter for the catalytically active site that is the metal nanoparticle. Engineering the structure of such ternary catalysts requires a high level of synthetic complexity, and in general, it is necessary to attain good dispersity of the transition metal species on the CeO_2, maximizing their net interfacial contact.[6]

The role of the carbon component as a support has not yet been investigated. Onion-like carbon (OLC) represents a unique class of nanostructured carbon materials with a quasi-spherical morphology, comprising multiple closed concentric shells of graphite/fullerene.[9] The unique physicochemistry of OLC such as high electrical conductivity ($2-4$ S cm^{-1}), high specific surface area ($200-600$ m^2 g^{-1}), very small nano-particulate sizes ($5-10$ nm), and high curvature and surface energy has allowed it to be utilized in enhancing the electrochemistry of some electrode materials in electro-catalysis, fuel cells, supercapacitors, and lithium-ion bat-teries.[10,11] Carbon−metal interactions are enhanced by the shape of OLC, which favors the interfacial contact between the two phases.[12] A direct consequence is an increased stabilization of supported small metal nanoparticles. This work describes an example of such effects. We report the preparation and full characterization of Pd−CeO_2−OLC materials investigated for the alkaline HOR. In AEMFC tests, the Pd−CeO_2−OLC hybrid exhibits a high activity equivalent to the acetylene black carbon-supported version. Importantly, Pd−CeO_2−OLC has enhanced stability in the operating fuel cell, due to strong charge transfer between the OLC and Pd−CeO_2 nanostruc-tures.

2. EXPERIMENTAL SECTION

2.1. Materials and Reagents. Acetylene carbon black, TIMICAL SUPER C45, 45 m^2 g^{-1}, was obtained from Gelon, China, while OLC was synthesized from high-purity (98−99%) nanodiamond powder (NaBond Technologies) by annealing in a muffle furnace at 1300 °C for 3 h in an argon atmosphere.[13] $PdCl_2$ (≥99.9%), ethylene glycol (99.8%), $Ce(NO_3)_3 \cdot 6H_2O$ (99.999%), and all other reagents were of analytical grade and purchased from Sigma-Aldrich without further purification. Platinum on graphitized carbon (40 wt %) was purchased from Sigma-Aldrich.

2.2. Synthesis Procedures. To allow for comparison, the synthesis methods used are similar to a previous report,[14] except those of the catalysts with OLC and OLC−CeO_2.

2.2.1. Synthesis of Pd/Carbon. A mixture of 0.25 g of conductive carbon black (CB, Timcal Super C45) and ethylene glycol (EG, 50 mL) was contained in a three-neck round-bottom flask (500 mL) and sonicated for 20 min. $PdCl_2$ (0.04165 mg) was dispersed in a mixture of H_2O (2.083 mL), EG (50 mL), and 0.25 mL of HCl (37%). The solution was then added in a dropwise fashion under stirring in a stream of N_2. After proper stirring, NaOH (5 g) was dissolved in H_2O (10 mL) and EG (35 mL) to make an alkaline solution, which was added to the reactor. The resultant mixture was then heated under a N_2 atmosphere for 3 h at 125 °C and then left to cool to room temperature. The mixture was then filtered, leaving behind the desired product, which was then rinsed with distilled H_2O until a neutral pH and then dried in a vacuum oven at 40 °C. The yields of Pd/CB and Pd/OLC were both 0.27 g.

2.2.2. Synthesis of Carbon−CeO_2 Support. A mixture of the carbon (2.0 g) and a solution of $Ce(NO_3)_3 \cdot 6H_2O$ (5.05 g) in H_2O (125 mL) was stirred for 60 min and sonicated for 30 min. The pH was then adjusted to 12 with KOH and stirred for 2 h. The mixture was then filtered, leaving behind the desired product, which was then rinsed with distilled H_2O until a neutral pH and then dried in a vacuum oven at 65 °C, and thereafter heated under air in a tube furnace for 2 h at 250 °C. The product was cooled to room temperature under a flow of Ar. The yield of CB−CeO_2 was 2.96 g, while the yield of OLC−CeO_2 was 2.51 g.

2.2.3. Synthesis of Pd−CeO_2/CB. CB−CeO_2 (250 mg) in water (31 mL) was vigorously stirred for 30 min and sonicated for 20 min. A solution of K_2PdCl_4 (86.25 mg) in water (3.75 mL) was then slowly added (approx. 1 h) while stirring. This was followed by the addition of an aqueous solution of 2.5 M KOH (0.525 mL), after which ethanol (50 mL) was added. The resulting mixture was heated for 60 min at 80 °C, after which it was filtered, leaving behind the desired product (Pd−CeO_2/CB), which was then rinsed several times with distilled water until a neutral pH and dried under a vacuum at 65 °C. The product (Pd−CeO_2/CB) yield was 0.275 g.

2.2.4. Synthesis of Pd−CeO_2/OLC. A suspension of OLC−CeO_2 (500 mg) in water (62.5 mL) was vigorously stirred for 30 min and sonicated for 20 min. A solution of K_2PdCl_4 (172.5 mg) in water (7.5 mL) was then slowly added (approx. 1 h) while stirring. This was followed by the addition of an aqueous solution of 2.5 M KOH (1.05 mL), after which ethanol (50 mL) was added. The resulting mixture was heated for 60 min at 80 °C, after which it was filtered, leaving behind the desired product (Pd−CeO_2/OLC), which was then washed with distilled water until a neutral pH and dried under a vacuum at 65 °C. The product (Pd−CeO_2/OLC) yield was 0.472 g.

2.3. Physical Property Characterization. The catalysts were characterized using powder X-ray diffraction (PXRD) (Bruker D2 Phaser X-ray diffractometer equipped with monochromatic Cu Kα X-rays at λ = 1.5406 Å) to investigate the crystallite size and structural phases. Elemental analysis of the samples was conducted using an energy-dispersive X-ray spectroscopy (EDS) unit "FEI Nova Nanolab 600 SEM" connected to a scanning electron microscope. This technique also establishes the chemical composition and elemental distribution profiles at the electrocatalyst surfaces. High-resolution transmission electron micrograms (HRTEM) were acquired from an HRTEM (JEOL 2010F). X-ray absorption fine structure (EXAFS) measurements on the coordination of the Pd−CeO_2−carbon system were acquired at beamline 5BM-D at the Advanced Photon Source. Scanning electron microscopy (SEM) and transmission electron microscopy (TEM) were used to obtain information on the structural properties of the samples and correlate it with Brunauer−Emmett−Teller (BET) results, while X-ray photoelectron spectroscopy (XPS) was employed to understand the chemical state and binding energies to within the surface resolution of the samples. The specific surface areas of the samples were obtained with the single-point Brunauer−Emmett−Teller (BET) method using a Micromeritics TriStar II 3000 area and porosity analyzer instrument. Raman spectroscopy (Bruker Senterra laser Raman spectrometer) was used to verify bond vibrations in Pd/CB, Pd−CeO_2/CB, Pd/OLC, and Pd−CeO_2/OLC. The thermal stability of each Pd-based sample was studied with the help of a Perkin Elmer Thermogravi-metric analyzer (TGA)/Differential Thermogravimetric Ana-
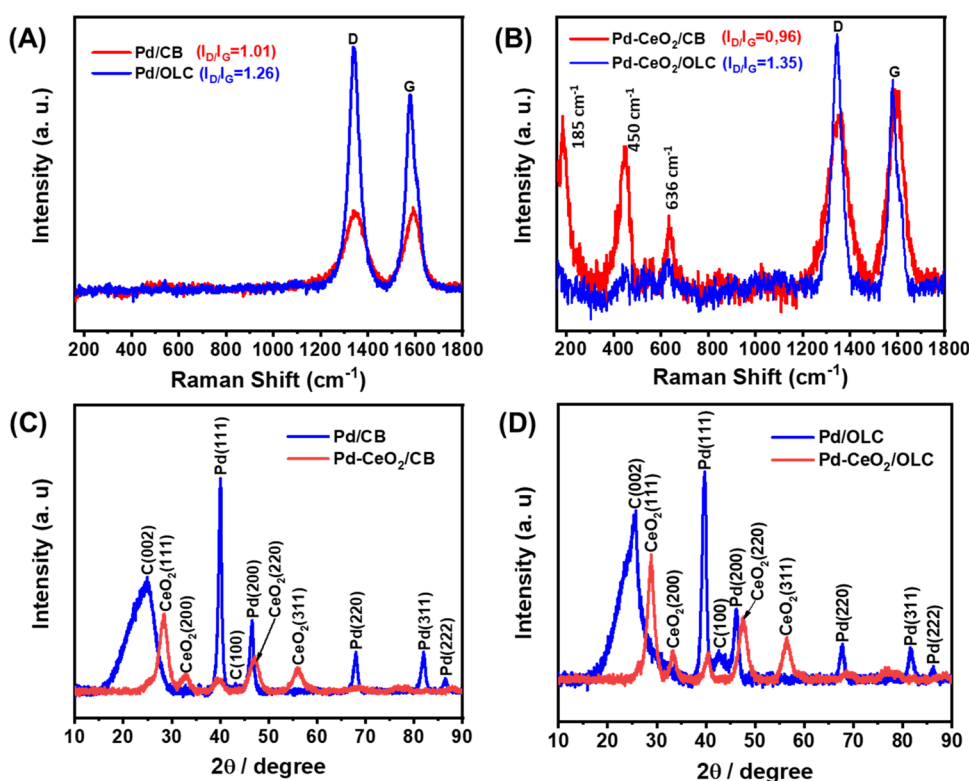
Figure 1. Raman spectra (A, B) and XRD patterns (C, D) of the electrocatalysts.

lyzer (DTGA) 6000. In a standard run, 10 mg of the samples was placed into a high-temperature alumina sample cup that was supported on an analytical balance located in the furnace chamber of the analyzer, and the sample was heated in the air (5 °C min^{-1}) from 35 to 900 °C. Initially, the instrument uses nitrogen gas for purging (20 mL min^{-1}) while holding at 35 °C for 5 min.

2.3.1. Density Functional Theory (DFT) Simulations. DFT simulations were performed at the supercomputational facilities at the Centre for High-Performance Computing (CHPC, Cape Town, South Africa) using the BIOVIA Materials Studio and employing an adsorption locator tool module.[15] Three adsorbates (H*, OH*, and OOH*) were chosen and adsorbed onto the modeled electrocatalyst surfaces (Pd/C, Pd/OLC, Pd/CeO$_2$/C, and Pd/CeO$_2$/OLC). Supercells of 3 × 3 were modeled for all of the above electrocatalysts, followed by geometric relaxation calculations with the threshold energy set at 10^{-6} eV for convergence to be achieved. The Materials Studio cleaning tool was used. The minimum adsorption distance was set at 5 Å. DMoI3, another module of the BIOVIA Materials Studio, was used to calculate the electronic properties. The same threshold energy as that used for adsorption was set for the calculations of electronic and energy properties. Condensed-phase optimization molecular potential for atomistic simulation studies (COMPASS) forcefield was used since it guarantees reliable theoretical results.

2.3.2. Electrochemical and Physical Characterization. Electrochemical measurements were used to examine the electrochemical performance of the synthesized electrocatalysts. The experiments were performed using an SP300 Bio-Logic Potentiostat (running on EC-Lab software). A three-electrode configuration was used for half-cell tests, comprising a glassy carbon electrode (GCE, diameter 5.0 mm, 0.196 cm^2)

modified with the electrocatalyst ink as the working electrode, a platinum wire as the counter electrode, and a Ag|AgCl electrode (3 M KCl) as the reference electrode. The GCE was cleaned by proper polishing on a pad using an alumina (Al$_2$O$_3$; nanopowder, Sigma-Aldrich) slurry followed by ultrasonic stirring in ethanol and acetone. The catalyst ink was prepared by dispersing the powder (1 mg) in ethanol (1 mL) and adding 100 μL of Nafion (5 wt %) to increase the adhesion of the catalyst material on the GCE. The mixture was sonicated for 30 min to obtain a homogeneous mixture. The catalyst ink (12 μL) was then deposited on the GCE in a dropwise fashion and allowed to dry, producing an electrocatalyst loading of 0.0144 mg cm^{-2}. Electrochemical impedance spectroscopy (EIS) was performed using a Bio-Logic Potentiostat between 100 kHz and 0.01 Hz at an amplitude of 10 mV in the electrolyte solution containing a redox probe (3 mM K$_4$Fe(CN)$_6$/K$_3$Fe(CN)$_6$ (1:1 mol ratio) dissolved in 0.1 M KCl). The EIS was conducted at an equilibrium potential ($E_{1/2}$) of the redox probe (0.15 V vs Ag|AgCl, 3 M KCl) observed from cyclic voltammetry experiments.

2.3.3. Fuel-Cell Testing. 2.3.3.1. Membrane-Electrode-Assembly (MEA) Preparation. The catalyst-coated gas diffusion electrode (GDE) method was used for fabricating the electrodes. First, ETFE-based RG-AEI powder (containing benzyltrimethylammonium (BTMA) functional groups with an ion-exchange capacity (IEC) of 1.26 ± 0.06 mmol g^{-1}) was ground with a pestle and mortar for 10 min. For each cathode GDE, the catalyst powder (Pt/C 40 wt %) and AEI powder (the latter always set to 20 wt % of the total solid mass) were mixed with 1 mL of water and 9 mL of propan-2-ol. This cathode catalyst ink was homogenized by ultrasonication for 30 min and then sprayed onto a Toray TGP-H-60 carbon paper gas diffusion substrate (Alfa Aesar, 10% PTFE) using an Iwata spray gun, with intermittent (<10 s) drying on a hot plate (80
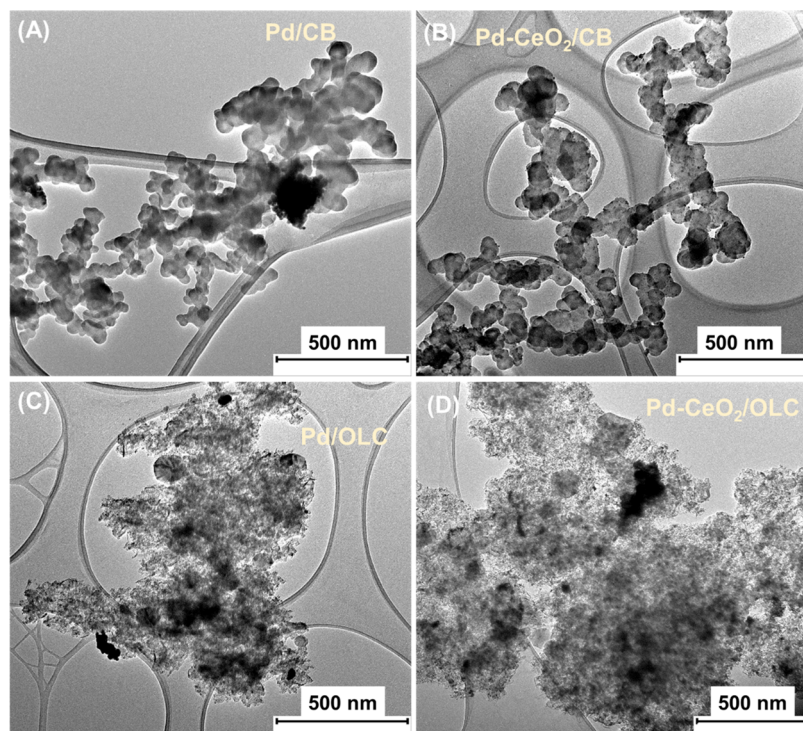
Figure 2. Typical low-resolution HRTEM images of (A) Pd/C, (B) Pd−CeO$_2$/CB, (C) Pd/OLC, and (D) Pd−CeO$_2$/OLC.

°C) and weighing to ensure the correct loadings. For the anode GDEs, each Pd catalyst was used to prepare electrodes (along with 20 wt % AEI). All electrodes and RG-AEMs (made from radiation grafting of 10 μM HDPE (electron-beamed to a 100 kGy absorbed dose) with a vinylbenzyl chloride monomer (mixture of 3- and 4-isomers) followed by amination with aqueous TMA (45% wt), IEC = 2.56 mmol g^{-1}) were immersed in an aqueous KOH solution (1 mol L^{-1}) for 1 h, with an exchange of the KOH solution with a fresh solution midway through, and then washed thoroughly in ultrapure water to remove excess KOH before assembly into a 5 cm^2 fuel-cell fixture (Scribner Associates) at a 5 N m torque.

2.3.3.2. Fuel-Cell Performance. An 850e fuel-cell test station (Scribner Associates) was used for testing. The fuel-cell temperature was varied between 60 and 80 °C. H$_2$ and O$_2$ gas feeds with flow rates of up to 1 and 2 L min^{-1} (SLPM) were supplied to the anode and cathode, respectively, with no back-pressurization. The dewpoints for both the anode and cathode gas supplies were adjusted to determine the sensitivity of performance to changes in gas humidification. All followers (heated lines between the fuel-cell tester and the fuel-cell fixture) were heated to prevent premature condensation before entry of the humidified gases into the flow field. The MEAs were activated by discharging the cell at a constant voltage of 0.5 V during cell heating and leaving the cells at this voltage until a steady current density was observed. AEMFC performance data were collected under controlled galvanostatic and potentiostatic conditions. The internal Ohmic resistances were estimated using the 850e instrument's internal current interrupt method.

3. RESULTS AND DISCUSSION

3.1. Material Characterization. Thermal stability analysis of the samples studied (Figure S1) has shown that Pd/CB and Pd/OLC retain approximately a 10 wt % Pd loading. Figure 1

compares the Raman spectra (Figure 1A,B) and PXRD patterns (Figure 1C,D) of the four materials.

The Raman spectra in all electrocatalysts exhibit the two characteristic peaks present carbon in the vicinity of 1000 cm^{-1} (D band, i.e., the defect or disorder band) and 2000 cm^{-1} (G band, i.e., the graphitization band). The D band is related to the disorder or defect induced by the C−C vibration (i.e., out-of-plane vibrations attributed to the sp^3-bonded carbon atoms), while the G band is related to the C═C graphite carbon vibration (i.e., in-plane displacement of sp^2-bonded carbon atoms).[16,17] The I_D/I_G intensity ratios were used to quantify the degree of disorder/crystallinity on the carbon support. The I_D/I_G values of Pd/CB, Pd−CeO$_2$/CB, Pd/OLC, and Pd−CeO$_2$/OLC have been calculated from their intensity ratios as 1.01, 0.96, 1.26, and 1.35, respectively (Table S1). These values suggest that (i) the OLC-supported electrocatalysts are more defective compared to their CB counterparts and (ii) CeO$_2$ is unable to oxidize CB but OLC is far more vulnerable. Indeed, the presence of CeO$_2$ in the Pd/CeO$_2$−OLC induced *ca.* 7% defects on the electrocatalysts. It is well established that imperfect (defect) surfaces efficiently modulate electron distribution for improved electrocatalytic activity than a perfect surface.[18−20] The intensity of a Raman band is dependent on several factors such as the cluster size and morphology of the material. Generally, inhomogeneity of strain and phonon confinement are known to be responsible for the broad and asymmetric character of the bands as the particle size gets smaller.[21−25] The Raman spectra of the CeO$_2$-based materials reveal some interesting phenomena. First, the band around 636 cm^{-1} is associated with the doubly degenerate LO mode of CeO$_2$,[23,24] and is linked to oxygen vacancies in the CeO$_2$ lattice.[25] This band is weaker for Pd/CeO$_2$−OLC, indicating that this material possesses more defects (oxygen vacancies: i.e., Pd−OLC$_x$Ce$_{1−x}$O$_{2−y}$) than its Pd/CeO$_2$−CB counterpart. Second, unlike the Pd/CeO$_2$−CB, the 450 cm^{-1}
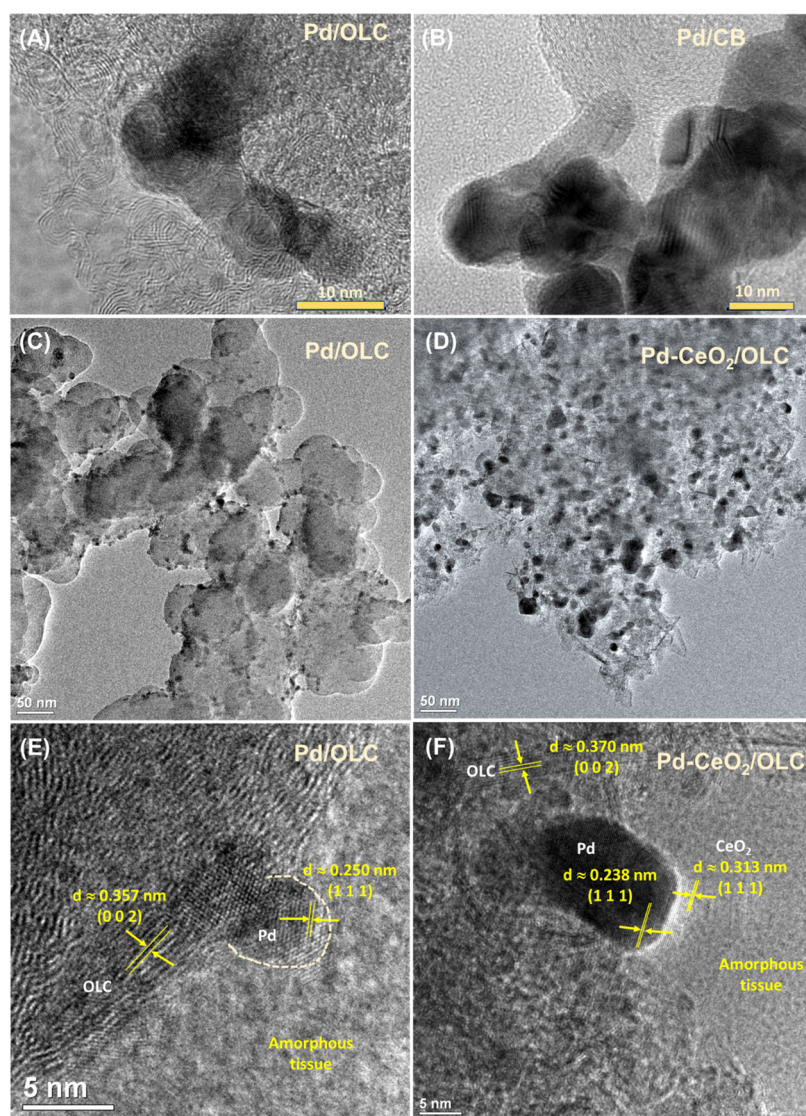
Figure 3. Typical HRTEM images of (A) Pd/OLC, (B) Pd/CB, (C, E) Pd/OLC, and (D, F) Pd−CeO$_2$/OLC.

peak is almost nonexistent. The disappearance of the 450 cm^{-1} peak has been attributed to the increased bond strength of the Pd−O−Ce bond.[21] Thus, in our case, this may be related to the increased bond strength of the Pd−O−Ce−OLC compared to the Pd−O−Ce−CB bond. Indeed, the observed weak or broad band in the 636 and 450 cm^{-1} regions is attributed to induced defects or disordering. Third, no band was observed below 400 cm^{-1} for Pd/CeO$_2$−OLC, while Pd/CeO$_2$−CB exhibits a well-defined peak at 185 cm^{-1}. The disappearance of bands below 400 cm^{-1} is associated with either the decrease of the crystallite size or phase stabilization.[21] Thus, in our case, it proves that Pd/CeO$_2$−OLC consists mostly of small nanocrystal sizes (confirmed by its high BET surface area, discussed later).

The PXRD patterns of the Pd catalysts confirm the successful synthesis of the nanocomposites. The hexagonal carbon structure (002) was observed at 2θ values of 24.3, 25.6, 25.9, and 26.1° for Pd/CB, Pd−CeO$_2$/CB, Pd/OLC, and Pd−CeO$_2$/OLC, respectively. The peaks due to palladium are recorded at 2θ ≈ 40, 47, 68, 82, and 86°, which are in good accordance with the FCC (face-centered cubic) structure of the crystal planes Pd(111), Pd(200), Pd(220), Pd(311), and

Pd(222), respectively. The Bragg reflections corresponding to an FCC phase of ceria are identified at 2θ = 28.7, 32.7, 47.3, 56.2, 69.1, 77.7, and 88.4°. These results agree with XRD patterns of Pd/C and Pd−CeO$_2$/C.[26,27] The diffraction peaks of Pd−CeO$_2$/CB and Pd−CeO$_2$/OLC are broader than their carbon-only supported counterparts, suggesting that the addition of ceria leads to smaller nanosized Pd particles. The carbon peak (002) is suppressed in the CeO$_2$-based catalyst because of the highly intense ceria peaks. The position of the peak (111) shifts to higher angles for the Pd−CeO$_2$/OLC sample because Pd moves into the ceria structure, causing the contraction of the unit cell and forming strong interaction between Pd and ceria.[28] Substitution of larger Ce^{4+}(0.97 Å) with smaller Pd^{2+} (0.86 Å) caused the characteristic peak (111) to shift to higher angles. Venkataswamy et al.[29] reported a similar shift to a higher angle with Cr-doped CeO$_2$ (where Cr is smaller than a Ce ion). Of interest is that the peak (111) for Pd−CeO$_2$/CB did not shift, whereas that of Pd−CeO$_2$/OLC shifted slightly (∼ 1 degree) to higher angles. Such a shift is usually attributed to lattice contraction; thus, as revealed by the Raman data, the strong interaction existing in OLC$_{x-}$Ce$_{1-x}$O$_{2-y}$ should be expected to exert a significant impact on the
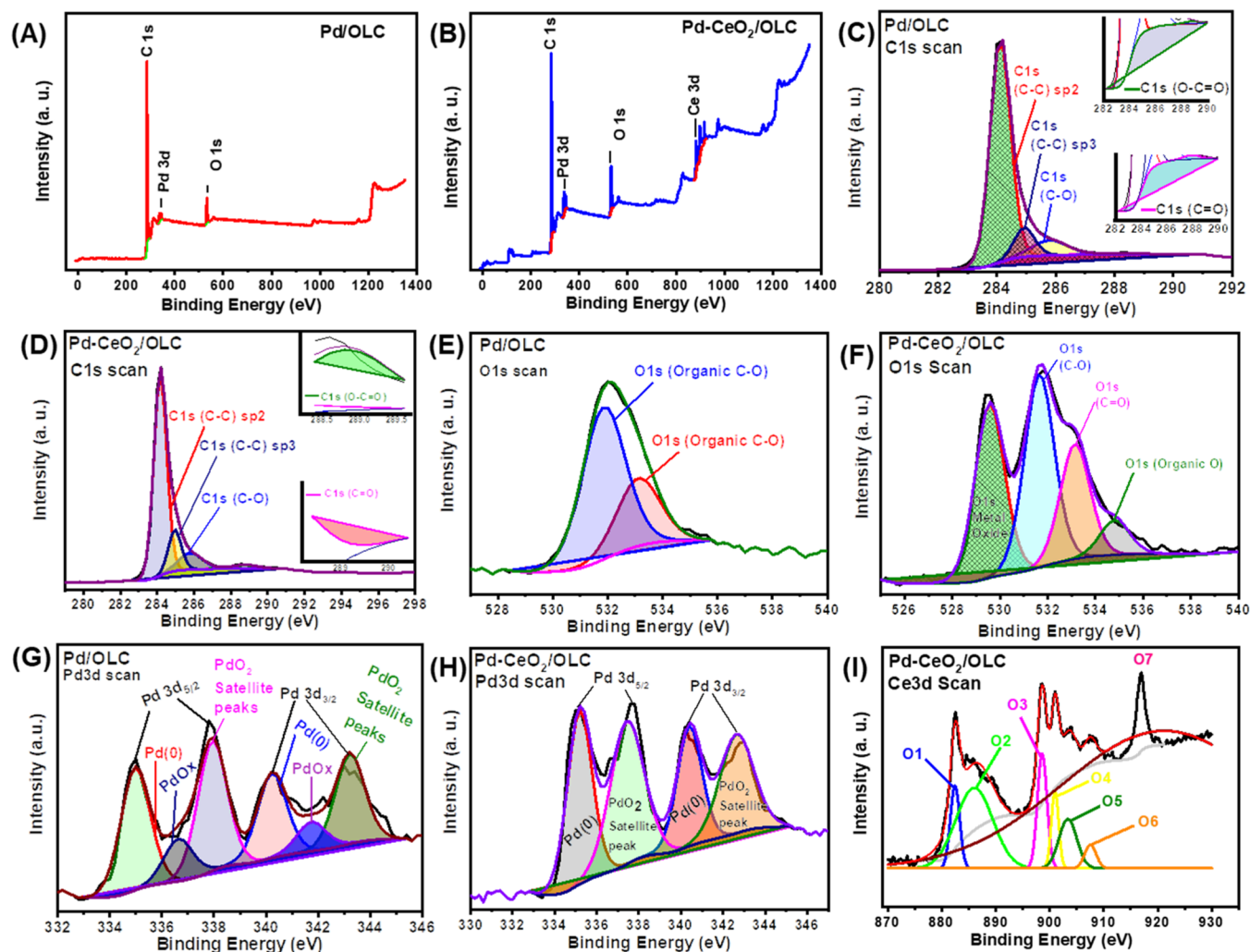
Figure 4. XPS data showing the wide spectra of (A) Pd/OLC and (B) Pd/CeO$_2$−OLC; C 1s scans of (C) Pd/OLC and (D) Pd−CeO$_2$/OLC; O 1s scans of (E) Pd/OLC and (F) Pd−CeO$_2$/OLC; Pd 3d scans of (G) Pd/OLC and (H) Pd−CeO$_2$/OLC; and Ce 3d scan of (I) Pd−CeO$_2$/OLC.

interaction with the Pd atom, hence the slight shift of the Pd(111) peak to a higher angle, i.e., contraction of the Pd−OLC$_x$−Ce$_{1−x}$O$_{2−y}$ lattice structure.

Figure 2 compares the low-resolution TEM images of the four catalysts (500 nm), which show that the OLC-based catalysts (Pd/OLC and Pd−CeO$_2$/OLC) exhibit a high surface area compared to the CB-based counterparts (Pd/CB and Pd−CeO$_2$/CB). To obtain further insights into the surface areas, the single-point BET method was adopted to calculate the specific surface area (SSA). The single-point BET method is a well-established method that allows for rapid and accurate determination of the specific surface area of materials,[30,31] including CeO$_2$−carbon-based materials.[31] The results are summarized in Table S2 and show that the SSA decreases as follows: Pd−CeO$_2$/OLC (373.53 m^2 g$^{−1}$) > Pd/OLC (357.73 m^2 g$^{−1}$) > Pd−CeO$_2$/CB (87.07 m^2 g$^{−1}$) > Pd/CB (30.57 m^2 g$^{−1}$), indicating that the OLC-based catalysts are 4−11 times higher than their CB-based counterparts. Importantly, the OLC-based electrocatalysts are mesoporous, while the CB-based are macroporous.

Figure 3 compares the HRTEM of the electrocatalysts. Pd/OLC (Figure 3A) clearly depicts the characteristic graphitic concentric rings or layers of the OLC, which are absent in the conventional carbon particles (Figure 3B). Pd/OLC exhibited

more dispersed Pd particles than Pd−CeO$_2$/OLC. Pd−CeO$_2$/OLC shows some agglomerated Pd particles of sizes up to 30 nm. For Pd/OLC (Figure 3E), the lattice fringes calculated as 0.250 and 0.357 nm were attributed to the Pd(111) and OLC(002), respectively. On the other hand, lattice fringes of Pd−CeO$_2$/OLC (Figure 3F) were determined as 0.370 nm attributed to OLC (002), 0.238 nm for Pd(111), and 0.313 nm for CeO$_2$ (111). This result suggests that the lattice fringes for the OLC expand with the addition of CeO$_2$. The expansion of the OLC lattice fringes in the presence of CeO$_2$ is consistent with the literature.[32] For example, Xu et al.[32b] reported that carbon onions exhibited a larger lattice spacing (0.372 nm compared to 0.342 nm) due to the formation of cracks between graphite layers arising from increased tensile stress. Thus, it may be reasonable to conclude that the presence of CeO$_2$ could have introduced some tensile stress onto the adjacent OLC, thereby leading to the cracking of some of the OLC graphite layers. Interestingly, the appearance of Pd(111) in intimate contact with CeO$_2$(111) confirms the Pd−CeO$_2$ interface and the possibility of lattice mismatch that could impact the strain energy, stabilize the interfacial structure, generate new electronic states in the band gap, and improve the electronic conductivity, and hence the electrocatalytic performance.

The particle size distribution of the catalysts (Figure S2) decreases as follows: Pd/C (52 nm) > Pd−CeO$_2$/CB (50 nm) ≫ Pd/OLC (7.5 nm) > Pd−CeO$_2$/OLC (6.2 nm), indicating that the OLC-based catalysts show the smallest nanoparticle sizes. This result corroborates their HRTEM images as well as the high specific surface areas from the single-point BET method.

XPS experiments were conducted for Pd/OLC and Pd−CeO$_2$/OLC. Wide surveys (Figure 4A,B) of the nanocatalyst surfaces reveal the expected elemental contents (i.e., Pd, Ce, O, and C). To further investigate the chemical environment of the constituent elements on the samples' surfaces, the spectrum corresponding to each element is deconvoluted. The deconvoluted C 1s spectra of the nanocatalysts confirm the chemical environments of the carbon support. Pd/OLC (Figure 4C) has C−C (sp^2), C−O, C=O, O−C=O, and C−C (sp^3) bonds at 284.1, 285.79, 287.9, 288.80, and 285 eV, respectively, whereas Pd−CeO$_2$/OLC (Figure 4D) has C−C (sp^2), C−O, C=O, O−C=O, and C−C (sp^3) bonds at 284.19, 285.79, 288.04, 288.80, and 285 eV, respectively. The deconvoluted O 1s spectra of the electrocatalysts are shown in Figure 4E,F. O 1s peaks appear at binding energies of 531.9 and 533.1 eV for Pd/OLC, attributed to the C−O and C=O organic bonds, respectively. For comparison, the O 1s peaks of Pd−CeO$_2$/OLC are observed at 529.6, 531.59, 533.19, and 534.8 eV, corresponding to metal oxide bonds, C−O organic, C=O organic bonds, and organic O, respectively. From the Pd 3d spectra (Figure 4G,H), the Pd/OLC peaks corresponding to Pd(0) 3d$_{5/2}$ and 3d$_{3/2}$ are observed at 335.0 and 340.0 eV, peaks at 336.6 and 341.8 eV correspond to Pd(II) 3d$_{5/2}$ and 3d$_{3/2}$, respectively, and those at 338 and 343.2 eV are attributed to PdO$_2$ 3d$_{5/2}$ and 3d$_{3/2}$, satellite peaks, respectively. For Pd−CeO$_2$/OLC, the peaks at 335.2 and 340.4 eV are assigned to Pd(0) 3d$_{5/2}$ and 3d$_{3/2}$, while those at 337.4 and 342.6 eV are attributed to PdO$_2$ 3d$_{5/2}$ and 3d$_{3/2}$ satellite peaks, respectively. Pd^{2+} (peak at 337.4 eV) at the interface could coordinate with the O$^{2−}$ of ceria, which may explain the Raman data on the inability of CeO$_2$ to oxidize OLC.

From the spectra of Ce 3d Pd−CeO$_2$/OLC (Figure 4I), the O1, O2, O3, O4, O5, O6, and O7 Ce (3d) signals are found at 882.4, 886, 898.6, 901, 903.4, 907.6, and 917 eV, respectively. The signals corresponding to Ce^{4+} 3d$_{3/2}$ and Ce^{4+} 3d$_{5/2}$ are observed at O7, O3, and O4, with binding energies of 917, 898.6, and 903.4 eV, respectively. The oxygen vacancies in CeO$_2$ make better dispersion of nanoparticles and favor the catalysis.[33] The O5 and O1 energy levels of Ce^{3+} 3d$_{3/2}$ and Ce^{3+} 3d$_{5/2}$ are at 903.4 and 882.4 eV, respectively. Two extra satellite peaks O6 and O2 are shown at 907.6 eV on Ce^{3+} 3d$_{3/2}$, and 886 eV on Ce^{3+} 3d$_{5/2}$, respectively. These results agree with previously reported spectra.[34]

Figure 5 shows the EXAFS data for Pd/OLC and Pd−CeO$_2$/OLC. The Athena code was used to extract the EXAFS oscillations and Arthemis software was employed for the analysis.[35] The amplitude reduction factor (S$_0^2$) and the photoelectron energy origin correction (ΔE$_0$) were found for the Pd foil and fixed for the samples as 0.8 and −6, respectively. The local environment of the Pd atoms was determined using the phase shift and amplitude functions of two Pd−O contributions and one Pd−Pd contribution. The Pd−O contributions were calculated using PdO with a tetragonal structure (CIF Collection Code 257583) and PdO with a cubic structure (CIF Collection Code 77650). The Pd−Pd contribution was calculated using a metallic Pd structure
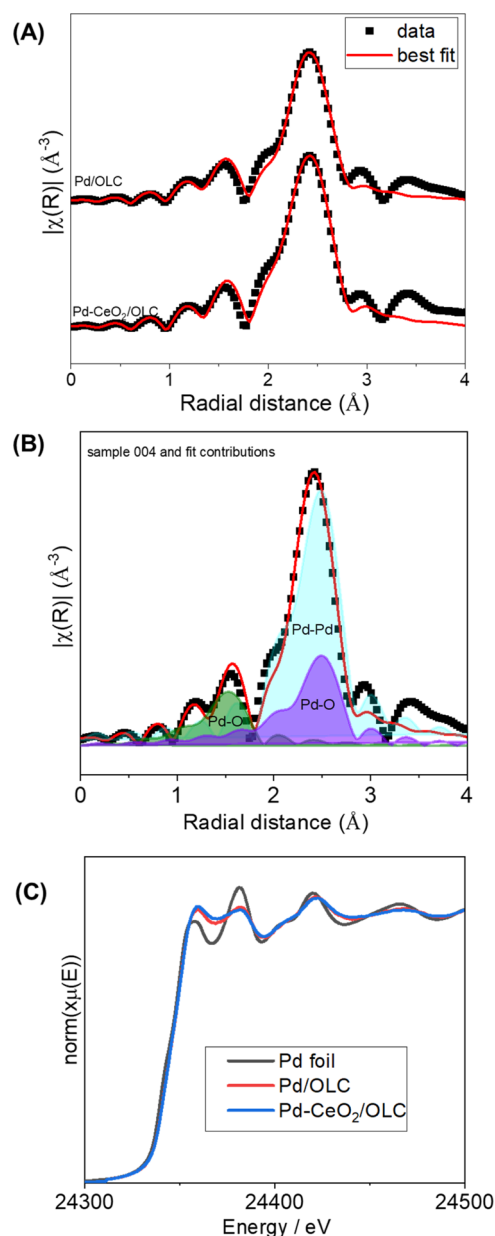

Figure 5. (A) Fourier transform of the k^2-weighted spectrum (not phase corrected) and the best fit for the Pd/OLC and Pd−CeO$_2$/OLC samples; (B) Fourier transforms, best fit, and fit contributions for the Pd/OLC sample; and (C) normalized XANES spectra at the Pd K-edge for all of the samples and metallic references.

(CIF Collection Code 257579). As a first attempt, the coordination numbers (N_i), distances (R_i), and the Debye−Waller factor (σ_i^2) of each path were adjusted freely and independently. However, the results for the σ_i^2 were very similar. Considering that the N_i and σ_i^2 are strongly correlated parameters, we opted to use the same σ_i^2 for all of the paths but continue adjusting it freely. In addition, a second model was tested using a second Pd−Pd contribution instead of the longer Pd−O contribution in the second shell. This attempt was made to test the presence of small PdO particles in addition to the metallic particles. The model did not represent the data. The range used to transform the EXAFS oscillations ($k^2\chi(k)$) was 3−12 and the interval where the fit was performed was 1−3 Å. Table 1 and Figure 5A present the fit results. Figure 5B presents the Pd/OLC fit and the

Table 1. Fit Results of the EXAFS Data[a]

	Pd−O contributions				metallic Pd	
	CN (Pd−O)	R (Å)	CN (Pd−O)	R (Å)	CN (Pd−Pd)	R (Å)
sample	4*	2.04*	6*	2.83*	12*	2.78*
Pd/OLC	1.7 ± 0.6	2.04 ± 0.03	7 ± 2	3.02 ± 0.03	5 ± 1	2.76 ± 0.005
Pd−CeO$_2$/OLC	1.7 ± 0.5	2.04 ± 0.02	8 ± 2	3.04 ± 0.001	6 ± 1	2.76 ± 0.01

[a]Key: CN = coordination number; * = expected value; and R = bonding length; σ_i^2 0.001 ± 0.001.

contributions. Both samples are very similar with only a small difference in the Pd−Pd contribution.

The samples' present coordination numbers for the Pd−Pd contribution are much smaller than what is expected for metallic bulk Pd (12). The Pd particles' dispersion increases in the order: Pd−CeO$_2$/OLC > Pd/OLC, with the CeO$_2$-based catalyst being the least dispersed sample, which is in good agreement with the HRTEM results. The Pd−O contributions are very similar and indicate the presence of highly dispersed Pd species in addition to the small Pd particles. From the EXAFS analysis, it is not possible to distinguish scattering from O, C, and N. Thus, the Pd−O contributions could be in fact due to Pd−C and Pd−O or Pd−N contributions. These contributions could come from an interaction with the carbon support and oxidation from the air or the reaction. From the XANES results (Figure 5C), we can observe that the samples are very similar to Pd^0 but with damped oscillations, characteristic of nanomaterials. A mixture of Pd and PdO is present in the sample, perhaps due to the Pd−O−Ce interaction. The chemical state of Pd and the atomic percentage of Pd^{2+} in the nanocomposites influence the performance of the catalyst.[36] The low coordination number of Pd−Pd could be related to the small nanoparticle size, porosity, and presence of surface defects in the OLC-based catalysts.

3.2. DFT Simulation for HOR. For the DFT calculations, Pd (111) was chosen as the model catalyst surface considering that the (111) plane is known to give the highest HOR activity among the low-index surfaces.[37] It is also the most prominent reflection in the XRD patterns. Also, the choice of Ce (111) and OLC (002) planes stems from their prevalence in the XRD patterns. The possible HOR intermediates (H*, OH*, and OOH*) were chosen as the adsorbates because they are well established, experimentally[38] and theoretically.[39] In the DFT calculation, the adsorption energy, E_{ad} (eV), is defined as (eq 1)

$$E_{ad} = (E_{surface+adsorbate}) - (E_{surface} + E_{adsorbate}) \tag{1}$$

where $E_{surface+adsorbate}$ represents the total energy of the interacting catalyst surface and the adsorbate, while $E_{surface} + E_{adsorbate}$ are the energies of the bare catalyst surface and the free adsorbate in the gas phase. According to this equation, a more negative E_{ad} value corresponds to stronger adsorption. For higher HOR activity, one expects that the best-performing electrocatalyst would possess a weaker adsorption strength with the adsorbates (i.e., H*, OH*, and OOH*). Thermodynamically, the more negative the ΔG value, the weaker the adsorbate on the electrocatalyst surface, thus the higher the HOR activity. The DFT results (summarized in Table 2) reveal that the both the E_{ad} and ΔG give the least negative values for the OLC-based electrocatalysts. In addition, conductivity increases (i.e., reduced energy band gap) as follows: Pd−CeO$_2$/OLC > Pd/OLC > Pd−CeO$_2$/OLC > Pd/

Table 2. Summary of Values of the Change in the Gibbs Free Energy (ΔG/eV), Adsorption Energy (E_{ad}/eV), and Energy Band Gap (E_g/eV) Obtained from DFT Calculations of the Electrocatalysts toward Possible HOR Intermediates (H*, OH*, and OOH*)

electrocatalyst	adsorbate	ΔG (eV)	E_{ad} (eV)	E_g (eV)
Pd/C				0.582
	H*	−1.787	−1.787	
	OH*	−5.087	−13.116	
	OOH*	−10.239	−39.856	
Pd/OLC				0.433
	H*	−0.838	−0.838	
	OH*	−2.418	−10.448	
	OOH*	−6.538	−36.155	
Pd−CeO$_2$/C				0.523
	H*	−1.042	−1.042	
	OH*	−3.395	−11.424	
	OOH*	−8.216	−37.833	
Pd−CeO$_2$/OLC				0.176
	H*	−0.272	−0.272	
	OH*	−2.106	−10.135	
	OOH*	−6.450	−36.067	

CB. This model predicts that the best-performing electrocatalyst (i.e., weak adsorption of the adsorbate and low band gap or high conductivity) is most likely to be Pd−CeO$_2$/OLC, while the poorest is Pd/CB. The predicted low band gap of Pd−CeO$_2$/OLC (0.176 eV) compared to Pd/OLC (0.433 eV) agrees with the Raman and HRTEM data; the presence of defects due to the CeO$_2$-engineered Pd−OLC interface is expected to provide a positive effect in the band gap and improve the electronic conductivity, and hence the electrocatalytic performance.

The intrinsic activity of the Pd-based electrocatalyst is intricately linked with its electronic structure. To understand the electronic properties of Pd/OLC before and after the incorporation of the CeO$_2$, we carried out calculations on the electronic band structures and the projected density of states (PDOS). As shown in Figure 6, before the incorporation of CeO$_2$, there are few available states in Pd/OLC (shown by the band structure, Figure 6A) compared to Pd−CeO$_2$/OLC (Figure 6C), which means that more electrons are available on Pd−CeO$_2$/OLC than on Pd/OLC alone.

This is further supported by the PDOS data (Figure 6B,D) where Pd/OLC indicates that only the electrons from the d-orbital of Pd are available (97.5 electrons/eV), while the PDOS of Pd−CeO$_2$/OLC emanates from the electrons of the OLC (p-orbital: 85 electrons/eV) and Pd (d-orbital: 93.7 electrons/eV). Thus, the electrons of Pd−CeO$_2$/OLC are nearly twice (~179 electrons/eV) those of Pd/OLC. This result suggests that the interaction of CeO$_2$ with Pd/OLC is due to the electron transfer process that leads to a mismatch in Fermi levels (E_f), decreasing from −3.517 to −4.373 eV. This
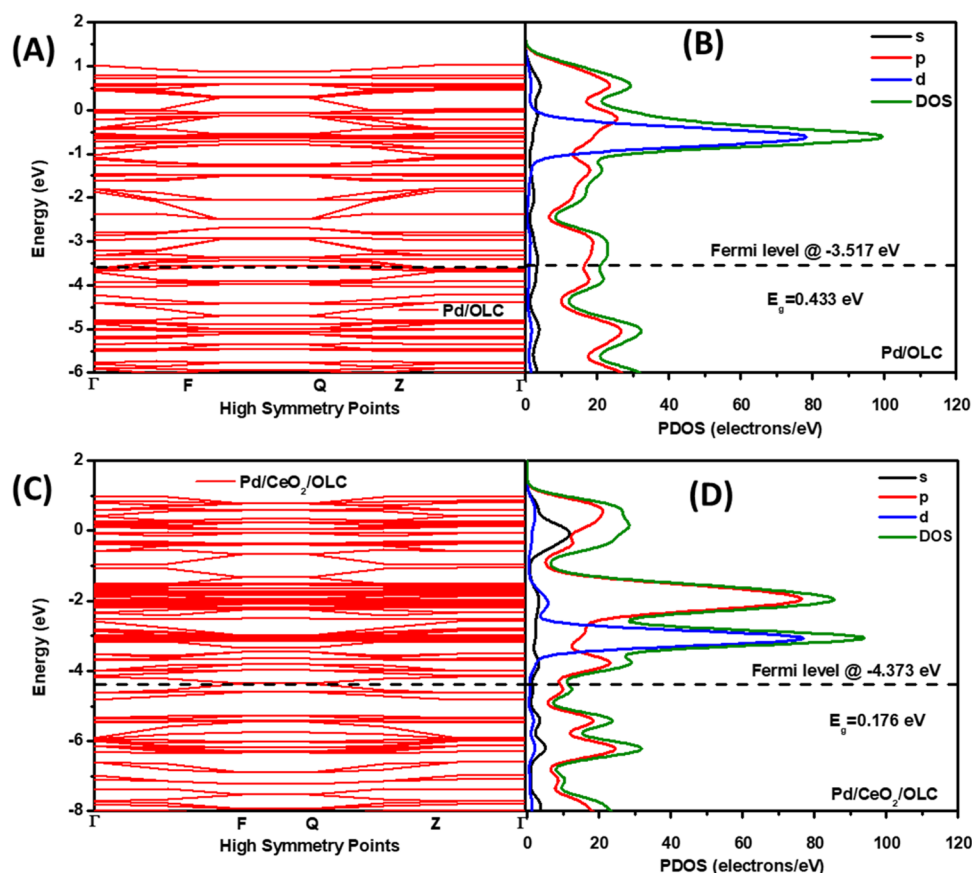
Figure 6. (A, C) Band structure and (B, D) partial density of states (PDOS) of (A, B) Pd/OLC and (C, D) Pd−CeO$_2$/OLC. The dotted lines represent the Fermi energy level and the energy band gap (E_g =0.433 eV for Pd/OLC and 0.176 eV for the Pd−CeO$_2$/OLC).

charge-transfer process leads to a redistribution of partial charge, which is likely to enhance the reactivity of Pd−CeO$_2$/OLC over its Pd/OLC counterpart toward HOR (as will be observed in the electrocatalytic section). The PDOS of Pd/OLC shows that the electrons in the conduction band are mainly from the d-orbital of Pd and Ce; however, the presence of CeO$_2$ enhances the electrons, incorporating both the d-orbital of Pd and the p-orbital of OLC.

3.3. Electrochemical Tests for HOR (Three-Electrode Cell). First, EIS was conducted with the four electrocatalysts to provide an insight into their charge-transfer process. EIS is an important tool for exploring the charge-transfer phenomena and conductivity of electrode materials.[40] The experimental Nyquist plots (Figure S3) were satisfactorily fitted with the electrical equivalent circuit (Figure S3 inset) comprising R_s (the electrolyte/solution resistance), R_{ct} (charge-transfer resistance), CPE (constant phase element), and the Warburg impedance (Wd). As summarized in Table S3, the value of R_{ct} decreases as Pd/CB (∼16 kΩ) > Pd−CeO$_2$/CB (∼3 kΩ) > Pd/OLC (∼2 kΩ) > Pd−CeO$_2$/OLC (∼0.8 kΩ), indicating that the OLC-based catalysts are the best-conducting materials, thus corroborating the DFT results.

Figure 7 summarizes the electrochemical performance of the four electrocatalysts. Cyclic voltammetry (CV) was performed on each of the Pd/CB, Pd/OLC, Pd−CeO$_2$/CB, and Pd−CeO$_2$/OLC electrode in N$_2$-saturated 0.5 M KOH (Figure 7A). Hydrogen adsorption/desorption peaks and palladium oxide (PdO) reduction peaks are observed between (0.35 and −0.07 V) and (0.52 and 0.85 V) vs RHE, respectively, for all of the electrocatalysts. The current densities of the hydrogen

adsorption/desorption peaks are much higher for the two electrocatalysts on CeO$_2$ support than those supported on carbon alone. Pd−CeO$_2$/OLC shows the highest PdO reduction peak around 0.67 V vs RHE. The PdO reduction peaks of the catalysts containing CeO$_2$ occur at earlier potential among others, which is an indication that less energy is needed to reduce PdO in the presence of CeO$_2$, which is possibly due to the attraction of Pd to metal oxides like CeO$_2$, which provide more oxygen to the Pd and PdO active sites, i.e., more difficult to reduce PdO oxides, as CeO$_2$ withdraws electrons from Pd. A similar observation was reported between Pd and SnO$_2$.[41]

The electrochemical active surface area (ECSA)$_{PdO}$ was estimated by integrating the PdO reduction peaks to find the Coulombic charge of each catalyst and then following the proposed method of Rand and Wood (eq 2)[42]

$$\text{ECSA} = \frac{Q}{S \cdot L} \tag{2}$$

where Q is the Coulombic charge (0.1662, 0.4054, 0.4498, and 0.8718 mC for Pd/CB, Pd−CeO$_2$/CB, Pd/OLC, and Pd−CeO$_2$/OLC, respectively), S is the Coulombic constant for a monolayer of Pd (0.424 mC cm^{-2}), and L is the electrocatalyst loading (∼1.0 μg (Pd)). The calculated ECSA$_{PdO}$ values decrease as follows: Pd−CeO$_2$/OLC (17.13 m^2 g$_{Pd}^{-1}$) > Pd−CeO$_2$/CB (8.84 m^2 g$_{Pd}^{-1}$) > Pd/OLC (7.67 m^2 g$_{Pd}^{-1}$) > Pd/CB (3.27 m^2 g$_{Pd}^{-1}$). These results reveal that CeO$_2$ acts as a promoter to boost the electrochemical activity of Pd in the supporting electrolyte, although Pd−CeO$_2$/OLC is the most active.
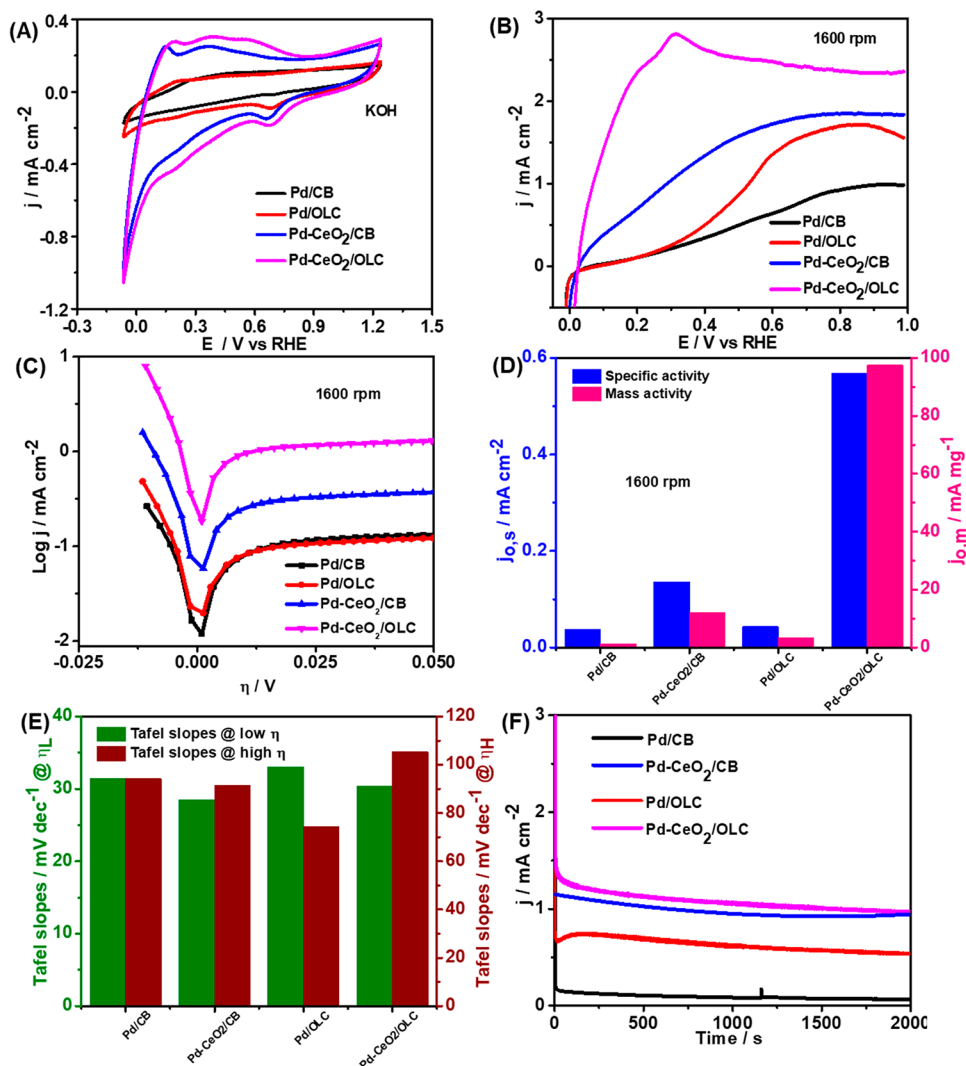
Figure 7. (A) CVs in 0.5 M KOH-purged N_2 at 50 mV s^{-1}, (B) LSV 1600 rpm at 5 mV s^{-1} in 0.5 M KOH-purged H_2, (C) Butler−Volmer plots, (D) specific and mass activities, (E) Tafel slopes (b_a) at low η and high η, and (F) CA at 0.2 V vs RHE of the electrocatalysts at 1600 rpm in 0.5 M KOH-saturated H_2.

The electrocatalysts were further investigated for HOR in H_2-saturated 0.5 M KOH at a sweep rate of 5 mV s^{-1} and 1600 rpm, as shown in the linear sweep voltammogram (LSV, Figure 7B). The LSVs of the electrocatalysts for HOR show that Pd−CeO_2/OLC has the highest limiting current response and also reaches the limiting current density at 0.2 V significantly before the other materials studied, followed by Pd−CeO_2/CB, Pd/OLC, and Pd/CB. Figure 7C shows the Butler−Volmer plots of the electrocatalysts where parameters such as mass ($j_{o,m}$) and specific ($j_{o,s}$) activities and Tafel slopes (b_a) at low (η_L) and high overpotentials (η_H) for HOR activity were extracted. Thus, the $j_{o,m}$ and $j_{o,s}$ for the electrocatalysts are Pd−CeO_2/OLC ($j_{o,m}$ = 97.49 mA mg^{-1}; $j_{o,s}$ = 0.569 mA cm^{-2}), Pd−CeO_2/CB ($j_{o,m}$ = 12.02 mA mg^{-1}; $j_{o,s}$ = 0.136 mA cm^{-2}), Pd/OLC ($j_{o,m}$ = 3.30 mA mg^{-1}; $j_{o,s}$ = 0.043 mA cm^{-2}), and Pd/CB ($j_{o,m}$ = 1.24 mA mg^{-1}; $j_{o,s}$ = 0.038 mA cm^{-2}), as shown in Figure 7D. Significantly increased HOR-specific activity was observed for Pd−CeO_2/OLC by 4.2, 13.2, and 15 times than those of Pd−CeO_2/CB, Pd/OLC, and Pd/CB, respectively. The enhanced HOR mass activity of Pd−CeO_2/OLC is traceable to its strong OH^- spillover/surface oxophilicity, ligand, strain, and synergistic effects of CeO_2 onto Pd. These

behaviors are common for cometals and their oxides for Pd electrocatalysts.[16,41,43] The mechanism of the electrocatalysts for HOR is determined from the magnitude of b_a at η_L and η_H. The Tafel slopes (Figure 7E) of the electrocatalysts at η_L (ca. 30 mV dec^{-1}) and η_H (74−105 mV dec^{-1}) correspond to the Tafel and Volmer steps, respectively. Similar observations were reported previously where the Volmer step is the rate-determining step (rds).[44,45] Hence, the HOR mechanism of the electrocatalysts followed the Tafel−Volmer mechanism. CA (Figure 7F) of the electrocatalysts revealed their stability during HOR at steady-state conditions. After 2000 s, the electrocatalysts with CeO_2 retain more current responses after their decay. The stability of the electrocatalysts was further corroborated with the accelerated durability test (ADT), i.e., LSV at 1600 rpm before and after 1000 cycled CV in H_2-saturated KOH, as shown in Figure S4. The ADT reveals degradation of 40, 29, 45, and 14% for Pd/CB, Pd/OLC, Pd−CeO_2/CB, and Pd−CeO_2/OLC, respectively. These results confirm that OLC is a unique platform for CeO_2 to not only improve the HOR activity but also durability. A similar observation has been previously reported.[46] The HOR

Table 3. HOR Data for the Electrocatalysts and Comparison with the Literature

| samples	ECSA ($m^2 \, g^{-1}$)	$j_{o,s}$ ($mA \, cm^{-2}$)	$j_{o,m}$ ($mA \, mg_{Pd}^{-1}$)	b_a ($mV \, dec^{-1}$) @ η_L	refs
Pd/CB	3.27	0.038	1.24	31.5 ± 3.7	this work
Pd—CeO$_2$/CB	8.84	0.136	12.02	28.5 ± 1.0	this work
Pd/OLC	7.67	0.043	3.30	33.1 ± 2.0	this work
Pd—CeO$_2$/OLC	17.13	0.569	97.49	30.4 ± 2.0	this work
Ru$_{0.80}$Pd$_{0.20}$	117.00	0.123	177.00	241.0	47
Pd$_{0.85}$Ru$_{0.15}$NTs	36.10	0.510	187.00	119.0	43
Pd/C—CeO$_2$ (Pd, 10 wt %)	43.00	0.055	24.00	66.0	7
Pd—CN$_x$	51.00	0.037	14.00	112.0	48
Pd—CeO$_2$/C (1:4:5)	63.00		20.00	70.0	8
Pd—CeO$_2$—25%	10.91	0.180	19.69		49
Pd/SnO$_2$/MOFDC	96.20	0.119	114.70	58.7 ± 9.7	50
Pt$_{0.9}$Pd$_{0.1}$/C	35.20	0.260	278.60		51
0.38 CeO$_x$-Pd/C	46.30	0.120	51.54	129.3	52
Pd/Ni-d/MOFDC	126.40	0.122	153.88	30.0 ± 3.8	4
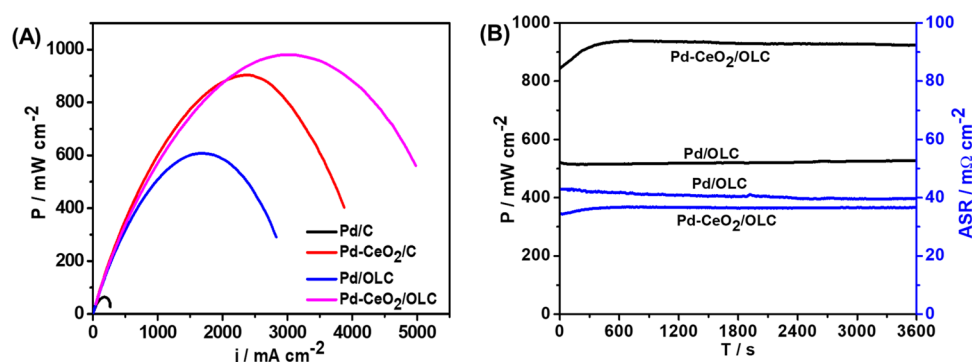
Figure 8. (A) Fuel-cell performance data at a high gas flow (1 (H$_2$) and 2 (O$_2$) L min^{-1}) and a cell temperature of 80 °C and (B) short 1 h test at 0.4 V for the Pd/OLC and Pd—CeO$_2$/CB samples. The ASR was monitored for the duration of each test.

activities of the electrocatalysts are summarized and compared with the literature in Table 3.

Mass transfer properties with regards to the kinetic and diffusion controlled-process of the electrocatalysts were investigated with LSV at different rotation speeds (400–2400 rpm), as shown in Figure S5. As the rotation speed increases, the limiting current response of the electrocatalysts increases concurrently, which is particularly more pronounced at the diffusion region of the polarization, i.e., 0.6 V for all. The Koutecky—Levich (Figure S6) representation of the LSV of the electrocatalysts displays linear plots, which were used to extract the mass transfer (i.e., heterogeneous rate constant, k) and diffusion parameters (i.e., diffusion coefficient, D) at varied overpotentials (0.65–0.85 V) from the intercepts and slopes, respectively. The D values of (1.07 ± 0.09, 1.21 ± 0.16, 1.36 ± 0.03, and 1.56 ± 0.06) × 10^{-5} cm^2 s^{-1} are measured for Pd/CB, Pd/OLC, Pd—CeO$_2$/CB, and Pd—CeO$_2$/OLC, with corresponding k values of 6.67 ± 1.59 × 10^{-3}, 3.63 ± 1.45 × 10^{-2}, 3.60 ± 0.44 × 10^{-2}, and 1.36 ± 0.20 × 10^{-1} cm s^{-1}, respectively. These results show that hydrogen diffuses rapidly on Pd—CeO$_2$/OLC at a faster rate during the HOR, followed by Pd—CeO$_2$/CB, Pd/OLC, and Pd/CB. The observations further corroborate the HOR-specific and mass activities of the electrocatalysts.

3.3.1. Anion-Exchange-Membrane Fuel-Cell Testing. The Pd-based anode catalysts were deposited at the desired loading (0.15 mg$_{Pd}$ cm^{-2}) onto a Teflon-treated Toray paper GDL by aerographic deposition of inks composed of catalyst particles and (insoluble) ionomer AEI powder (20 wt % dry).

Commercial Pt/C (40 wt %) was used to prepare the cathode electrodes (0.4 mg$_{Pt}$ cm^{-2}). Prior to cell testing, the (AEI-containing) electrodes and HDPE-AEM were soaked in an aqueous 1.0 M KOH solution for 1 h to displace Cl$^-$ counter ions to predominantly OH$^-$ anions (with trace HCO$_3^-$/CO$_3^{2-}$ due to adsorption of CO$_2$ from the air) in the AEM. The electrodes and HDPE-AEM were then washed with ultrapure water to remove excess K$^+$ cations and OH$^-$ counter ions before assembly in the fuel-cell hardware. The HDPE-AEM was sandwiched between the anode and cathode electrodes and pressed between the graphite flow fields using appropriate gaskets to optimize the compression and sealing. The exact test conditions used to obtain fuel-cell data are summarized in each figure caption. All gases were supplied without back-pressurization. The MEAs were "activated" via operation at 0.5 V until a steady current density was achieved (minimum of 1 h). During the experiments, the cell temperature, gas humidification, and flow regime were adjusted to reach a suitably stable cell performance. Initially, the fuel-cell performance was determined under conditions of high temperature (80 °C) and high gas flow regimes (1 and 2 slm for anode (H$_2$) and cathode (O$_2$), respectively), as shown in Figure 8A. A clear performance improvement can be observed when CeO$_2$ is combined with both the carbon types (CB and OLC).

The ameliorative effect of intimate Pd—CeO$_2$ interactions on the alkaline HOR is now well documented.[14,53] The catalysts with OLC-type carbon exhibit further enhancements in both peak power density (1.0 W cm^{-2} for Pd—CeO$_2$/OLC) and current density at 0.1 V (5.0 A cm^{-2} for Pd—CeO$_2$/OLC).

A summary of important fuel-cell data is shown in Table 4. Such results are consistent with the electrochemical tests,

Table 4. Summary of AEMFC Test Conditions and Key Performance Parameters (with the Pt/C Cathode Containing 0.4 mg$_{Pt}$ cm^{-2}, All Electrodes Containing 20 wt % ETFE-Based RG-AEI with Inks Sprayed on Toray TGP-H-60 10% PTFE, HDPE-Based RG-AEM ca. 25 μm Thick When Hydrated)

anode	P/W cm^{-2} @ 0.6 V (j/A cm^{-2})	P_{max}/W cm^{-2} (j/A cm^{-2})	current density @ 0.1 V cell (j/A cm^{-2})
Pd/C	0.04 (0.07)	0.05 (0.1)	0.05
Pd/OLC	0.37 (0.61)	0.6 (1.7)	3.0
Pd−CeO$_2$/C	0.60 (1.0)	0.9 (2.2)	4.0
Pd−CeO$_2$/OLC	0.50 (0.83)	1.0 (3.0)	5.0

which show better HOR activity when CeO$_2$ is integrated with the carbon in the support, and the best HOR activity is shown for the Pd−CeO$_2$/OLC sample. At a constant cell voltage of 0.4 V, both Pd/OLC and Pd−CeO$_2$/OLC fuel cells have a stable beginning of the life power output (Figure 8B). Pd−CeO$_2$/OLC operates at 900 mW cm^{-2} compared to 500 mW cm^{-2} for Pd/OLC over an initial 1 h time frame. The area-

specific resistance (ASR) was similar for both cells (<40 mΩ cm^{-2}), suggesting that the performance improvement with CeO$_2$ is due to better kinetics. Pd−CeO$_2$/OLC has a lower ASR despite the presence of the poorly electron-conducting CeO$_2$ incorporated into the catalyst.

At a more realistic gas flow regime (H$_2$ 0.5 and O$_2$ 1 L min^{-1}), we studied both OLC-containing catalysts and the Pd−CeO$_2$/C material at various cell temperatures and gas humidification (Figure 9A−C), and the results confirm that Pd−CeO$_2$/C and Pd−CeO$_2$/OLC exhibit higher activity under all test conditions. The fuel cells that have CeO$_2$ integrated on the anode electrode perform better at low H$_2$ gas humidification (66%), suggesting that these anodes favor the back diffusion of water through the membrane to the cathode where it is consumed during the ORR. These anodes may also suffer from anode flooding at high humidification and such a phenomenon could be a cause of the performance loss. State-of-the-art commercial PtRu/C anode catalysts perform best at higher RHs (90−100%).[54] For example, a 2000 h stability test of a PtRu/C MEA was undertaken at 90% RH and showed only a 3.65% performance loss.[55] Cell performance was monitored over 15 h for each OLC-based catalyst at a fixed cell voltage of 0.4 V (T_{cell} 80 °C, T_{hum} 70 °C, RH 66%) (Figure 9D−F). The cells were stopped (overnight period)
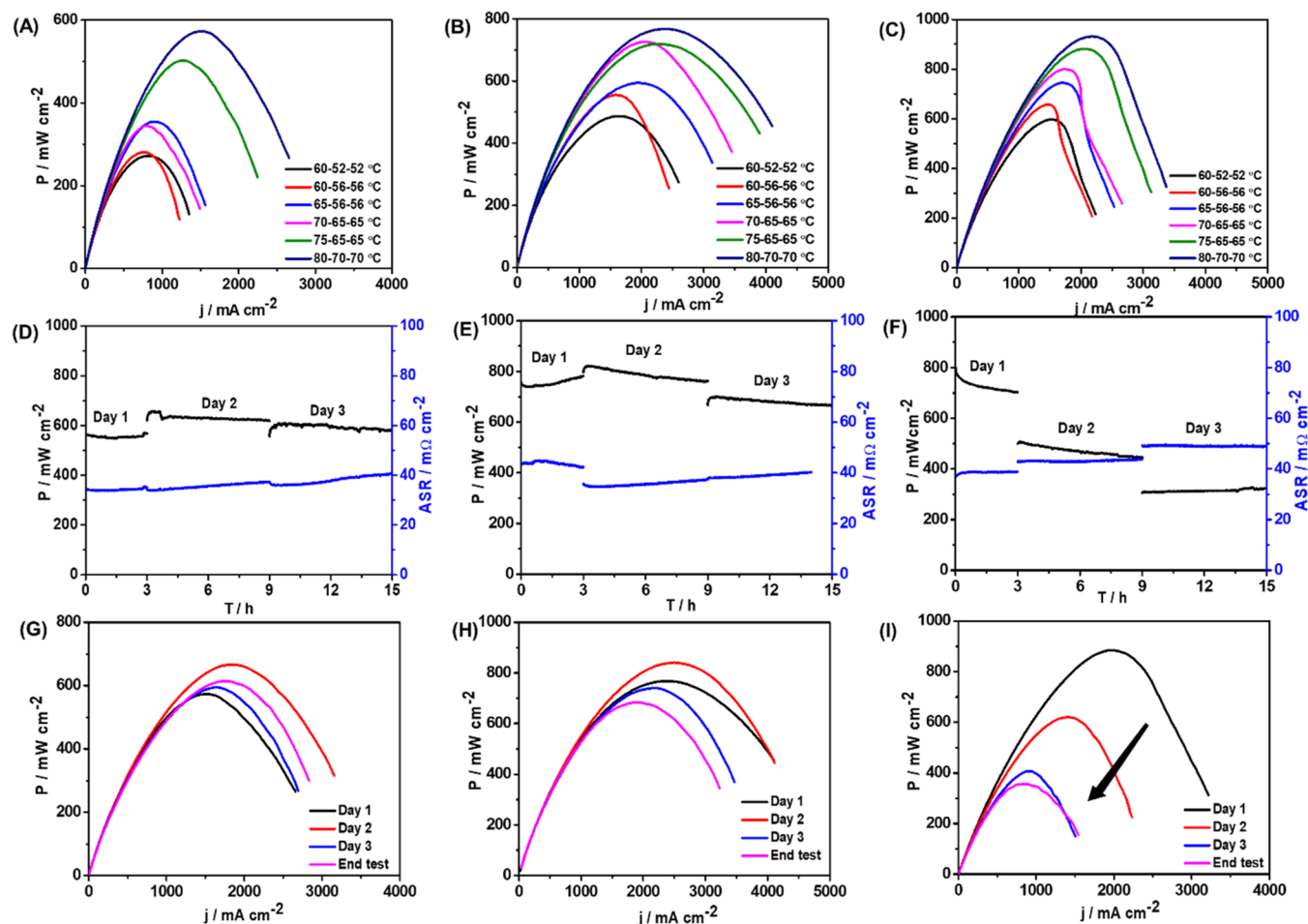

Figure 9. AEMFC data with Pd/OLC (A, D, G), Pd−CeO$_2$/OLC (B, E, H), and Pd−CeO$_2$/CB (C, F, I) anode catalysts (0.15 mg cm^{-2} Pd loading), cathode Pt/C (0.4 mg cm^{-2}), and HDPE-AEM. Both cathode and anode electrodes contain 20 wt % ETFE-based RG-AEI powder. (A, B, C) Effect of cell temperature and gas humidification on cell performance. (D, E, F) Test at a 0.4 V constant and (G, H, I) PD curves measured periodically during constant 0.4 V tests (T_{cell} 80 °C RH 66% both gases).

after 3, 9, and 15 h testing and fuel-cell curves were measured to observe the performance loss. The best performance for the Pd/OLC cell was 650 mW cm^{-2} during the test and remained generally stable (only 80 mW cm^{-2} drop over 15 h), whereas for Pd−CeO$_2$/OLC, the cell power output dropped from a high value of 840 mW cm^{-2} by around 180 mW cm^{-2} over a period of the test. The series of fuel-cell curves confirms a greater loss of performance for the Pd−CeO$_2$/OLC cell showing also that losses were not recoverable after each stop. Performance does remain significantly higher for the Pd−CeO$_2$/OLC catalyst throughout the testing. The area-specific cell resistance (ASR) was monitored during testing, and the results are also plotted in Figure 9D−F. A clear coupling of power density to changes in ASR can be seen with increases in ASR associated with lower power density during the test. Under the same test conditions, the Pd−CeO$_2$/C anode (Figure 9C,F,I) displayed higher initial performance (peak power >900 mW cm^{-2}), and at the same time, suffered from mass transport losses at higher current densities. Interestingly, during the constant potential cell test over 3 days, the cell suffered a much more severe loss of performance reaching 300 mW cm^{-2}. The OLC-based anodes maintained their performances, suggesting a net in-operando stabilization of the Pd−CeO$_2$ catalyst when supported on OLC. Cyclic voltammetry-accelerated stress testing also confirms the improved stability of Pd−CeO$_2$ when supported on OLC.

4. CONCLUSIONS

This study entails the preparation of Pd−CeO$_2$/OLC, Pd/OLC electrocatalysts, and their carbon black (CB) analogues. Robust characterization of the electrocatalysts with Raman, XRD, XPS, EXAFS, TGA, BET, EDS, SEM, and TEM reveals physicochemical properties such as a large BET surface area, pore volume, and small Pd particle size, as well as enhanced interfacial interaction and synergy among Pd, CeO$_2$, and OLC in Pd−CeO$_2$/OLC that are beneficial for improved electrocatalysis. Hence, theoretical and experimental studies of the electrocatalysts for HOR and AEMFC are presented. In the theoretical context prior to the adsorption of absorbates (H*, OH*, and OOH*) onto the electrocatalysts, Pd−CeO$_2$/OLC has the lowest band gap (E_g = 0.179 eV) compared to Pd−CeO$_2$/CB (E_g = 0.523 eV), Pd/OLC (E_g = 0.433 eV), and Pd/CB (E_g = 0.582 eV). This result shows that there is synergy among the constituents of Pd−CeO$_2$/OLC for improved conductivity. Also, the adsorption and Gibbs free energies of the absorbates on the electrocatalysts decrease in the following trend Pd−CeO$_2$/OLC > Pd/OLC > Pd−CeO$_2$/OLC > Pd/CB, which align with the experimental data. In the three-electrode configuration, Pd−CeO$_2$/OLC exhibits an outstanding HOR activity (i.e., high ECSA, $j_{o,s}$, $j_{o,m}$, k, and D, and low E_{onset}) and stability compared to Pd−CeO$_2$/CB, Pd/OLC, and Pd/CB. In the AEMFC with H$_2$ fuel, Pd−CeO$_2$/OLC delivers a high peak power density of 1.0 mW cm^{-2} at 3.0 A cm^{-2} relative to Pd−CeO$_2$/CB (0.9 mW cm^{-2} at 2.2 A cm^{-2}), Pd/OLC (0.6 mW cm^{-2} at 1.7 A cm^{-2}), and Pd/CB (0.05 mW cm^{-2} at 0.1 A cm^{-2}). Moreover, catalysts containing OLC are more stable than CB-based catalysts. This study, therefore, reveals the unique roles of CeO$_2$ in the Pd−OLC interface to rationally synthesize high-performance and durable anode electrocatalysts for AEMFC.

■ ASSOCIATED CONTENT

ⓢ Supporting Information

The Supporting Information is available free of charge at https://pubs.acs.org/doi/10.1021/acscatal.2c01863.

> TGA, summary of Raman data, BET data, particle size distribution (histogram), electrochemical impedance spectra (Nyquist plots) and data table, LSV at 1600 rpm before and after 1000 cycles ADT for the anion-exchange-membrane fuel cell, LSV at different rotation speeds, and Koutecky−Levich plots at different over-potentials (PDF)

■ AUTHOR INFORMATION

Corresponding Authors

Daniel M. Wamwangi − *School of Physics, University of the Witwatersrand, Johannesburg 2050, South Africa;* Email: daniel.wamwangi@wits.ac.za

Kenneth I. Ozoemena − *School of Chemistry, Molecular Sciences Institute, University of the Witwatersrand, Johannesburg 2050, South Africa;* ● orcid.org/0000-0001-7107-7003; Email: kenneth.ozoemena@wits.ac.za

Authors

Jimodo J. Ogada − *School of Physics, University of the Witwatersrand, Johannesburg 2050, South Africa; School of Chemistry, Molecular Sciences Institute, University of the Witwatersrand, Johannesburg 2050, South Africa*

Adewale K. Ipadeola − *School of Chemistry, Molecular Sciences Institute, University of the Witwatersrand, Johannesburg 2050, South Africa*

Patrick V. Mwonga − *School of Chemistry, Molecular Sciences Institute, University of the Witwatersrand, Johannesburg 2050, South Africa*

Aderemi B. Haruna − *School of Chemistry, Molecular Sciences Institute, University of the Witwatersrand, Johannesburg 2050, South Africa*

Forrest Nichols − *Department of Chemistry and Biochemistry, University of California, Santa Cruz, California 95064, United States*

Shaowei Chen − *Department of Chemistry and Biochemistry, University of California, Santa Cruz, California 95064, United States;* ● orcid.org/0000-0002-3668-8551

Hamish A. Miller − *Institute of Chemistry of Organometallic Compounds − National Research Council of Italy (ICCOM-CNR), 50019 Sesto Fiorentino (Florence), Italy;* ● orcid.org/0000-0003-1668-6476

Maria V. Pagliaro − *Institute of Chemistry of Organometallic Compounds − National Research Council of Italy (ICCOM-CNR), 50019 Sesto Fiorentino (Florence), Italy*

Francesco Vizza − *Institute of Chemistry of Organometallic Compounds − National Research Council of Italy (ICCOM-CNR), 50019 Sesto Fiorentino (Florence), Italy;* ● orcid.org/0000-0003-3850-0249

John R. Varcoe − *Department of Chemistry, University of Surrey, Surrey GU2 7XH, U.K.*

Debora Motta Meira − *CLS@APS Sector 20, Advanced Photon Source, Argonne National Laboratory, Argonne, Illinois 60439, United States; Canadian Light Source Inc., Saskatoon, Saskatchewan S7N 2V3, Canada;* ● orcid.org/0000-0002-7529-2736

Complete contact information is available at:
https://pubs.acs.org/10.1021/acscatal.2c01863

Author Contributions

K.I.O. contributed to the conception, interpretation of data, writing, and supervision of students; D.M.W. contributed to interpretation of data, writing, and cosupervision of students; J.J.O. contributed to experimentation, interpretation of data, and writing; A.K.I. contributed to experimentation, interpretation of data, and writing; F.N. contributed to HRTEM experiments and review; S.C. contributed to acquisition of EXAFS and HRTEM, interpretation of data, and writing; A.H. contributed to experimentation, interpretation of data, and writing; P.M. contributed to DFT modeling/calculations, interpretation, and writing; H.A.M. contributed to experimentation on AEMFC, interpretation of data, and writing; M.V.P. contributed to experimentation on AEMFC, interpretation of data, and writing; F.V. contributed to experimentation on AEMFC, interpretation of data, and review; J.R.V. contributed to the synthesis and characterization of the anion-exchange membrane and review; and D.M.M. contributed to fitting of EXAFS data and interpretation and writing. All authors have given approval to the final version of the manuscript.

Notes

The authors declare no competing financial interest.

■ ACKNOWLEDGMENTS

■ REFERENCES

(1) Saikia, K.; Kakati, B. K.; Boro, B.; Verma, A. Current Advances and Applications of Fuel Cell Technologies. In *Recent Advancements in Biofuels and Bioenergy Utilization*, Springer, 2018; pp. 303−337.

(2) Wang, Y.; Yuan, H.; Martinez, A.; Hong, P.; Xu, H.; Bockmiller, F. R. Polymer electrolyte membrane fuel cell and hydrogen station networks for automobiles: Status, technology, and perspectives. *Adv. Appl. Energy* **2021**, *2*, No. 100011.

(3) (a) Dekel, D. R. Review of cell performance in anion exchange membrane fuel cells. *J. Power Sources* **2018**, *375*, 158−169. (b) Mustain, W. E. Understanding how high-performance anion exchange membrane fuel cells were achieved: Component, interfacial, and cell-level factors. *Curr. Opin. Electrochem.* **2018**, *12*, 233−239.

(4) Ipadeola, A. K.; Mwonga, P. V.; Ozoemena, K. I. Hydrogen oxidation and oxygen reduction reactions on palladium nano-electrocatalyst supported on nickel-deficient MOF-derived carbons. *Electrochim. Acta* **2021**, *390*, No. 138860.

(5) Omasta, T. J.; Zhang, Y.; Park, A. M.; Peng, X.; Pivovar, B.; Varcoe, J. R.; Mustain, W. E. Strategies for reducing the PGM loading in high power AEMFC anodes. *J. Electrochem. Soc.* **2018**, *165*, F710.

(6) Miller, H. A.; Bellini, M.; Dekel, D. R.; Vizza, F. Recent developments in Pd-CeO2 nano-composite electrocatalysts for anodic reactions in anion exchange membrane fuel cells. *Electrochem. Commun.* **2022**, *135*, No. 107219.

(7) Miller, H. A.; Vizza, F.; Marelli, M.; Zadick, A.; Dubau, L.; Chatenet, M.; Geiger, S.; Cherevko, S.; Doan, H.; Pavlicek, R. K.; et al. Highly active nanostructured palladium-ceria electrocatalysts for the hydrogen oxidation reaction in alkaline medium. *Nano Energy* **2017**, *33*, 293−305.

(8) Bellini, M.; Pagliaro, M. V.; Lenarda, A.; Fornasiero, P.; Marelli, M.; Evangelisti, C.; Innocenti, M.; Jia, Q.; Mukerjee, S.; Jankovic, J.; et al. Palladium−ceria catalysts with enhanced alkaline hydrogen oxidation activity for anion exchange membrane fuel cells. *ACS Appl. Energy Mater.* **2019**, *2*, 4999−5008.

(9) Mykhailiv, O.; Zubyk, H.; Plonska-Brzezinska, M. E. Carbon nano-onions: Unique carbon nanostructures with fascinating properties and their potential applications. *Inorg. Chim. Acta* **2017**, *468*, 49−66.

(10) Zeiger, M.; Jäckel, N.; Aslan, M.; Weingarth, D.; Presser, V. Understanding structure and porosity of nanodiamond-derived carbon onions. *Carbon* **2015**, *84*, 584−598.

(11) Zeiger, M.; Jäckel, N.; Mochalin, V. N.; Presser, V. carbon onions for electrochemical energy storage. *J. Mater. Chem. A* **2016**, *4*, 3172−3196.

(12) Chen, X.; Li, J. Superlubricity of carbon nanostructures. *Carbon* **2020**, *158*, 1−23.

(13) Hantel, M. M.; Presser, V.; McDonough, J.; Feng, G.; Cummings, P. T.; Gogotsi, Y.; Kötz, R. In situ electrochemical dilatometry of onion-like carbon and carbon black. *J. Electrochem. Soc.* **2012**, *159*, A1897.

(14) Miller, H. A.; Vizza, F.; Marelli, M.; Zadick, A.; Dubau, L.; Chatenet, M.; Geiger, S.; Cherevko, S.; Doan, H.; Pavlicek, R. K.; et al. Highly active nanostructured palladium-ceria electrocatalysts for the hydrogen oxidation reaction in alkaline medium. *Nano Energy* **2017**, *33*, 293−305.

(15) Ipadeola, A. K.; Mwonga, P. V.; Ray, S. C.; Maphanga, R. R.; Ozoemena, K. I. Bifunctional Behavior of Pd/Ni Nanocatalysts on MOF-Derived Carbons for Alkaline Water-splitting. *Electroanalysis* **2020**, *32*, 3060−3074.

(16) Ipadeola, A. K.; Lisa Mathebula, N. Z.; Pagliaro, M. V.; Miller, H. A.; Vizza, F.; Davies, V.; Jia, Q.; Marken, F.; Ozoemena, K. I. Unmasking the Latent Passivating Roles of Ni (OH) 2 on the Performance of Pd−Ni Electrocatalysts for Alkaline Ethanol Fuel Cells. *ACS Appl. Energy Mater.* **2020**, *3*, 8786−8802.

(17) (a) Mofokeng, T. P.; Ipadeola, A. K.; Tetana, Z. N.; Ozoemena, K. I. Defect-engineered nanostructured Ni/MOF-derived carbons for an efficient aqueous battery-type energy storage device. *ACS Omega* **2020**, *5*, 20461−20472. (b) Li, J.-G.; Tsai, C.-Y.; Kuo, S.-W. Fabrication and characterization of inorganic silver and palladium nanostructures within hexagonal cylindrical channels of mesoporous carbon. *Polymers* **2014**, *6*, 1794−1809.

(18) Jiao, S.; Fu, X.; Wang, S.; Zhao, Y. Perfecting electrocatalysts via imperfections: towards the large-scale deployment of water electrolysis technology. *Energy Environ. Sci.* **2021**, *14*, 1722−1770.

(19) He, G.; Song, Y.; Liu, K.; Walter, A.; Chen, S.; Chen, S. Oxygen reduction catalyzed by platinum nanoparticles supported on graphene quantum dots. *ACS Catal.* **2013**, *3*, 831−838.

(20) Song, Y.; Chen, S. Graphene quantum-dot-supported platinum nanoparticles: defect-mediated electrocatalytic activity in oxygen reduction. *ACS Appl. Mater. Interfaces* **2014**, *6*, 14050−14060.

(21) Loridant, S. Raman spectroscopy as a powerful tool to characterize ceria-based catalysts. *Catal. Today* **2021**, *373*, 98−111.

(22) (a) Reddy, B. M.; Khan, A.; Yamada, Y.; Kobayashi, T.; Loridant, S.; Volta, J.-C. Surface characterization of CeO2/SiO2 and V2O5/CeO2/SiO2 catalysts by Raman, XPS, and other techniques. *J. Phys. Chem. B* **2002**, *106*, 10964−10972. (b) Spanier, J. E.; Robinson, R. D.; Zhang, F.; Chan, S.-W.; Herman, I. P. Size-dependent properties of CeO 2− y nanoparticles as studied by Raman scattering. *Phys. Rev. B* **2001**, *64*, No. 245407.

(23) Lin, X.-M.; Li, L.-P.; Li, G.-S.; Su, W.-H. Transport property and Raman spectra of nanocrystalline solid solutions Ce0. 8Nd0. 2O2−δ with different particle size. *Mater. Chem. Phys.* **2001**, *69*, 236−240.

(24) Weber, W. H.; Hass, K.; McBride, J. Raman study of CeO 2: Second-order scattering, lattice dynamics, and particle-size effects. *Phys. Rev. B* **1993**, *48*, 178.

(25) McBride, J. R.; Hass, K.; Poindexter, B.; Weber, W. Raman and x-ray studies of Ce1− x RE x O2− y, where RE = La, Pr, Nd, Eu, Gd, and Tb. *J. Appl. Phys.* **1994**, *76*, 2435−2441.

(26) Bambagioni, V.; Bianchini, C.; Chen, Y.; Filippi, J.; Fornasiero, P.; Innocenti, M.; Lavacchi, A.; Marchionni, A.; Oberhauser, W.; Vizza, F. Energy Efficiency Enhancement of Ethanol Electrooxidation on Pd−CeO2/C in Passive and Active Polymer Electrolyte-Membrane Fuel Cells. *ChemSusChem* **2012**, *5*, 1266−1273.

(27) Bianchini, C.; Shen, P. K. Palladium-based electrocatalysts for alcohol oxidation in half cells and in direct alcohol fuel cells. *Chem. Rev.* **2009**, *109*, 4183−4206.

(28) Li, K.; Lyu, T.; He, J.; Jang, B. W. Selective hydrogenation of acetylene over Pd/CeO2. *Front. Chem. Sci. Eng.* **2020**, *14*, 929−936.

(29) Venkataswamy, P.; Damma, D.; Jampaiah, D.; Mukherjee, D.; Vithal, M.; Reddy, B. M. Cr-doped CeO2 nanorods for CO oxidation: insights into promotional effect of Cr on structure and catalytic performance. *Catal. Lett.* **2020**, *150*, 948−962.

(30) Dollimore, D.; Spooner, P. A single point method for evaluating the specific surface area of a solid from nitrogen adsorption isotherms. *J. Appl. Chem. Biotechnol.* **1974**, *24*, 35−41.

(31) Khan, M. E.; Khan, M. M.; Cho, M. H. Ce3+-ion, surface oxygen vacancy, and visible light-induced photocatalytic dye degradation and photocapacitive performance of CeO2-graphene nanostructures. *Sci. Rep.* **2017**, *7*, No. 5928.

(32) (a) Li, J.; Wang, N.; Deng, J.; Qian, W.; Chu, W. Flexible metal-templated fabrication of mesoporous onion-like carbon and Fe 2 O 3@ N-doped carbon foam for electrochemical energy storage. *J. Mater. Chem. A* **2018**, *6*, 13012−13020. (b) Xu, J.; Zhang, R.; Wang, J.; Ge, S.; Wen, F. Hollow carbon onions with larger lattice spacing obtained by chlorination of the ball-milled SiC. *Mater. Lett.* **2012**, *88*, 168−170.

(33) Wang, J.; Li, B.; Yersak, T.; Yang, D.; Xiao, Q.; Zhang, J.; Zhang, C. Recent advances in Pt-based octahedral nanocrystals as high performance fuel cell catalysts. *J. Mater. Chem. A* **2016**, *4*, 11559−11581.

(34) (a) Arumugam, A.; Karthikeyan, C.; Hameed, A. S. H.; Gopinath, K.; Gowri, S.; Karthika, V. Synthesis of cerium oxide nanoparticles using Gloriosa superba L. leaf extract and their structural, optical and antibacterial properties. *Mater. Sci. Eng.: C* **2015**, *49*, 408−415. (b) Wang, G.; Mu, Q.; Chen, T.; Wang, Y. Synthesis, characterization and photoluminescence of CeO2 nanoparticles by a facile method at room temperature. *J. Alloys Compd.* **2010**, *493*, 202−207.

(35) Ravel, B.; Newville, M. ATHENA, ARTEMIS, HEPHAESTUS: data analysis for X-ray absorption spectroscopy using IFEFFIT. *J. Synchrotron Radiat.* **2005**, *12*, 537−541.

(36) (a) Luo, M.; Guo, S. Strain-controlled electrocatalysis on multimetallic nanomaterials. *Nat. Rev. Mater.* **2017**, *2*, 1−13. (b) Mavrikakis, M.; Hammer, B.; Nørskov, J. K. Effect of strain on the reactivity of metal surfaces. *Phys. Rev. Lett.* **1998**, *81*, 2819.

(37) Takehiro, N.; Liu, P.; Bergbreiter, A.; Nørskov, J. K.; Behm, R. J. Hydrogen adsorption on bimetallic PdAu (111) surface alloys: minimum adsorption ensemble, ligand and ensemble effects, and ensemble confinement. *Phys. Chem. Chem. Phys.* **2014**, *16*, 23930−23943.

(38) Ramaswamy, N.; Ghoshal, S.; Bates, M. K.; Jia, Q.; Li, J.; Mukerjee, S. Hydrogen oxidation reaction in alkaline media: Relationship between electrocatalysis and electrochemical double-layer structure. *Nano Energy* **2017**, *41*, 765−771.

(39) Feng, Z.; Li, L.; Zheng, X.; Li, J.; Yang, N.; Ding, W.; Wei, Z. Role of hydroxyl species in hydrogen oxidation reaction: a DFT study. *J. Phys. Chem. C* **2019**, *123*, 23931−23939.

(40) (a) Adekunle, A. S.; Ozoemena, K. I. Electron transfer behaviour of single-walled carbon nanotubes electro-decorated with nickel and nickel oxide layers. *Electrochim. Acta* **2008**, *53*, 5774−5782. (b) Pillay, J.; Ozoemena, K. I. Layer-by-layer self-assembled nanostructured phthalocyaninatoiron (II)/SWCNT-poly (m-amino-benzenesulfonic acid) hybrid system on gold surface: Electron transfer dynamics and amplification of H2O2 response. *Electrochim. Acta*

2009, *54*, 5053−5059. (c) Agboola, B. O.; Ozoemena, K. I. Self-assembly and heterogeneous electron transfer properties of metallo-octacarboxyphthalocyanine complexes on gold electrode. *Phys. Chem. Chem. Phys.* **2008**, *10*, 2399−2408. (d) Ozoemena, K. I.; Mathebula, N. S.; Pillay, J.; Toschi, G.; Verschoor, J. A. Electron transfer dynamics across self-assembled N-(2-mercaptoethyl) octadecana-mide/mycolic acid layers: impedimetric insights into the structural integrity and interaction with anti-mycolic acid antibodies. *Phys. Chem. Chem. Phys.* **2010**, *12*, 345−357. (e) Chidembo, A. T.; Ozoemena, K. I.; Agboola, B. O.; Gupta, V.; Wildgoose, G. G.; Compton, R. G. Nickel (II) tetra-aminophthalocyanine modified MWCNTs as potential nanocomposite materials for the development of supercapacitors. *Energy Environ. Sci.* **2010**, *3*, 228−236. (f) Lekitima, J. N.; Ozoemena, K. I.; Jafta, C. J.; Kobayashi, N.; Song, Y.; Tong, D.; Chen, S.; Oyama, M. High-performance aqueous asymmetric electrochemical capacitors based on graphene oxide/cobalt (ii)-tetrapyrazinoporphyrazine hybrids. *J. Mater. Chem. A* **2013**, *1*, 2821−2826. (g) Raju, K.; Ozoemena, K. I. Hierarchical one-dimensional ammonium nickel phosphate microrods for high-performance pseudocapacitors. *Sci. Rep.* **2015**, *5*, No. 17629.

(41) Ipadeola, A. K.; Barik, R.; Ray, S. C.; Ozoemena, K. I. Bimetallic Pd/SnO 2 nanoparticles on metal organic framework (MOF)-derived carbon as electrocatalysts for ethanol oxidation. *Electrocatalysis* **2019**, *10*, 366−380.

(42) Rand, D.; Woods, R. The nature of adsorbed oxygen on rhodium, palladium and gold electrodes. *J. Electroanal. Chem. Interfacial Electrochem.* **1971**, *31*, 29−38.

(43) St John, S.; Atkinson, R. W., III; Unocic, K. A.; Unocic, R. R.; Zawodzinski, T. A., Jr.; Papandrew, A. B. Platinum and palladium overlayers dramatically enhance the activity of ruthenium nanotubes for alkaline hydrogen oxidation. *ACS Catal.* **2015**, *5*, 7015−7023.

(44) Arulrajan, A. C.; Subramanian, P.; Singh, R. K.; Schechter, A. Pd-Decorated Tungsten as Pt-Free Bimetallic Catalysts for Hydrogen Oxidation Reaction in Alkaline Electrolyte. *Isr. J. Chem.* **2020**, *60*, 563−569.

(45) Zheng, J.; Zhou, S.; Gu, S.; Xu, B.; Yan, Y. Size-dependent hydrogen oxidation and evolution activities on supported palladium nanoparticles in acid and base. *J. Electrochem. Soc.* **2016**, *163*, F499.

(46) Speck, F. D.; Ali, F. S.; Paul, M. T.; Singh, R. K.; Böhm, T.; Hofer, A.; Kasian, O.; Thiele, S.; Bachmann, J.; Dekel, D. R.; et al. Improved Hydrogen Oxidation Reaction Activity and Stability of Buried Metal-Oxide Electrocatalyst Interfaces. *Chem. Mater.* **2020**, *32*, 7716−7724.

(47) St John, S.; Atkinson, R. W., III; Unocic, R. R.; Zawodzinski, T. A., Jr.; Papandrew, A. B. Ruthenium-alloy electrocatalysts with tunable hydrogen oxidation kinetics in alkaline electrolyte. *J. Phys. Chem. C* **2015**, *119*, 13481−13487.

(48) Bhowmik, T.; Kundu, M. K.; Barman, S. Palladium nano-particle−graphitic carbon nitride porous synergistic catalyst for hydrogen evolution/oxidation reactions over a broad range of pH and correlation of its catalytic activity with measured hydrogen binding energy. *ACS Catal.* **2016**, *6*, 1929−1941.

(49) Yarmiayev, V.; Alesker, M.; Muzikansky, A.; Zysler, M.; Zitoun, D. Enhancement of Palladium HOR Activity in Alkaline Conditions through Ceria Surface Doping. *J. Electrochem. Soc.* **2019**, *166*, F3234.

(50) Ipadeola, A. K.; Mwonga, P. V.; Ray, S. C.; Maphanga, R. R.; Ozoemena, K. I. Palladium/Stannic Oxide Interfacial Chemistry Promotes Hydrogen Oxidation Reactions in Alkaline Medium. *ChemElectroChem* **2020**, *7*, 4562−4571.

(51) Zhao, T.; Wang, G.; Gong, M.; Xiao, D.; Chen, Y.; Shen, T.; Lu, Y.; Zhang, J.; Xin, H.; Li, Q.; Wang, D. Self-Optimized Ligand Effect in L12-PtPdFe Intermetallic for Efficient and Stable Alkaline Hydrogen Oxidation Reaction. *ACS Catal.* **2020**, *10*, 15207−15216.

(52) Singh, R. K.; Davydova, E. S.; Douglin, J.; Godoy, A. O.; Tan, H.; Bellini, M.; Allen, B. J.; Jankovic, J.; Miller, H. A.; Alba-Rubio, A. C.; Alba-Rubio, A. C. Synthesis of CeOx-Decorated Pd/C Catalysts by Controlled Surface Reactions for Hydrogen Oxidation in Anion Exchange Membrane Fuel Cells. *Adv. Funct. Mater.* **2020**, *30*, No. 2002087.

(53) (a) Miller, H. A.; Pagliaro, M. V.; Bellini, M.; Bartoli, F.; Wang, L. Q.; Salam, I.; Varcoe, J. R.; Vizza, F. Integration of a Pd-CeO2/C Anode with Pt and Pt-Free Cathode Catalysts in High Power Density Anion Exchange Membrane Fuel Cells. *Acs Applied Energy Materials* **2020**, *3*, 10209−10214. (b) Miller, H. A.; Lavacchi, A.; Vizza, F.; Marelli, M.; Di Benedetto, F.; Acapito, F. D. I.; Paska, Y.; Page, M.; Dekel, D. R. A Pd/C-CeO2 Anode Catalyst for High-Performance Platinum-Free Anion Exchange Membrane Fuel Cells. *Angew. Chem. Int. Ed.* **2016**, *55*, 6004−6007.

(54) Yang-Neyerlin, A. C.; Medina, S.; Meek, K. M.; Strasser, D. J.; He, C.; Knauss, D. M.; Mustain, W. E.; Pylypenko, S.; Pivovar, B. S. Editors' Choice-Examining Performance and Durability of Anion Exchange Membrane Fuel Cells with Novel Spirocyclic Anion Exchange Membranes. *J. Electrochem. Soc.* **2021**, *168*, No. 044525.

(55) (a) Ul Hassan, N.; Mandal, M.; Huang, G. R.; Firouzjaie, H. A.; Kohl, P. A.; Mustain, W. E. Achieving High-Performance and 2000 h Stability in Anion Exchange Membrane Fuel Cells by Manipulating Ionomer Properties and Electrode Optimization. *Adv. Energy Mater.* **2020**, *10*, No. 2001986. (b) Mustain, W. E.; Chatenet, M.; Page, M.; Kim, Y. S. Durability challenges of anion exchange membrane fuel cells. *Energy Environ. Sci.* **2020**, *13*, 2805−2838.

■ NOTE ADDED AFTER ASAP PUBLICATION

This paper was originally published ASAP on May 31, 2022. Due to a production error, Figure 7D contained incorrect y-axis labels. The revised version was reposted on June 2, 2022.